Eddy Dynamics in a Primitive Equation Model: Sensitivity to Horizontal Resolution and Friction

CLAUS W. BÖNING AND REINHARD G. BUDICH

Institut für Meereskunde an der Universität Kiel, Germany

(Manuscript received 29 March 1991, in final form 25 July 1991)

ABSTRACT

A primitive equation model of an idealized ocean basin, driven by simple, steady wind and buoyancy forcing at the surface, is used to study the dynamics of mesoscale eddies. Model statistics of a six-year integration using a fine grid ($1/6° \times 0.2°$), with reduced coefficients of horizontal friction, are compared to those using a coarser grid ($1/3° \times 0.4°$), but otherwise identical configuration. Eddy generation in both model cases is primarily due to the release of mean potential energy by baroclinic instability. Horizontal Reynolds stresses become significant near the midlatitude jet of the fine-grid case, with a tendency for preferred energy transfers from the eddies to the mean flow. Using the finer resolution, eddy kinetic energy nearly doubles at the surface of the subtropical gyre, and increases by factors of 3–4 over the jet region and in higher latitudes. The spatial characteristics of the mesoscale fluctuations are examined by calculating zonal wavenumber spectra and velocity autocorrelation functions. With the higher resolution, the dominant eddy scale remains approximately the same in the subtropical gyre but decreases by a factor of 2 in the subpolar areas. The wavenumber spectra indicate a strong influence of the model friction in the coarse-grid case, especially in higher latitudes. Using the coarse grid, there is almost no separation between the energetic eddy scale and the scale where friction begins to dominate, leading to steep spectra beyond the cutoff wavenumber. Using the finer resolution an inertial subrange with a k^{-3} power law begins to emerge in all model regions outside the equatorial belt.

Despite the large increase of eddy intensity in the fine-grid model, effects on the mean northward transport of heat are negligible. Strong eddy fluxes of heat across the midlatitude jet are almost exactly compensated by changes of the heat transport due to the mean flow.

1. Introduction

The kinetic energy of the geostrophic flow field in the ocean is dominated by mesoscale eddies with spatial scales of about, in midlatitudes, 50–200 km. A question of particular importance to the ocean's role in climate is the influence of the energetic fluctuations on the large-scale transports of heat and momentum. During the past 15 years it has been a primary objective of eddy-resolving general circulation models (EGCMs) to understand the role of the eddies in the mean dynamic balances. However, examination of the influence of the oceanic eddies on large-scale transport processes still suffers from the compromises that have to be made due to the heavy demands of computing power necessary to represent the mesoscale variability in numerical models of planetary scale.

One option is to favor gridpoint resolution and compromise potentially important physics of the ocean dynamics by adopting a simpler set of equations and choose basin sizes small compared to the real oceans. Extensive use has been made of quasigeostrophic (QG) models to investigate the generation of mesoscale eddies in simplified ocean basins and their dynamical interaction with the mean flow. Reviews are given by Holland et al. (1983) and Holland (1985). A crucial parameter in these models is the horizontal grid spacing; it implies, for numerical reasons, a minimum value for the coefficient of horizontal friction. Substantial effects on mean flow and eddy properties are found even when decreasing the grid size from 20 to 10 km (Barnier et al. 1991).

A still simplified, but geophysically sized basin, and the more complete physics of the primitive equations (PE), were used by Cox (1985; hereafter C85) in a study of eddy effects on transport processes in the subtropical thermocline. Eddies generated by baroclinic instability in the westward-flowing portion of the gyre led to strongly enhanced mixing of the ventilated water masses and homogenization of properties over large areas of the thermocline (Böning and Cox 1988). Bryan (1987) has pointed out that the inclusion of thermohaline dynamics led to fundamental differences in the distribution of isopycnal potential vorticity compared to the QG case, and noted various common features with oceanic fields in the PE solution. However, the model generalization had to come at the expense of grid resolution ($1/3°$ meridional $\times$ $0.4°$ zonal), allowing the representation of only the upper range of the mesoscale eddies.

Corresponding author address: Dr. Claus Böning, Institut fur Meereskunde, Düsternbrooker Weg 20, D-2300 Kiel 1, Germany.

Recently, several investigations into the role of eddies in the circulation of realistic ocean basins, driven by realistic forcing fields, had been initiated: the U.K. fine-resolution model of the Southern Ocean (FRAM Group 1991); the model of the World Ocean of Semtner and Chervin (1988); and the "community modeling effort" (CME) of the World Ocean Circulation Experiment (WOCE). The first experiment within that effort, a simulation of the North and equatorial Atlantic Ocean, had been set up by Bryan and Holland (1989), based on the same PE code (Bryan 1969), the same grid size (1/3° × 0.4°), and similar values for the coefficients of horizontal friction as in the box model of C85 (Table 1). A sequence of experiments using this configuration, with different choices for the forcing functions and frictional parameters, had been performed at NCAR and at IfM Kiel (Böning et al. 1991). Evaluations of various aspects of the model solutions show that this model configuration is quite successful in reproducing many details of the hydrographic structure and current fields of the Atlantic Ocean (Spall 1990; Schott and Böning 1991; Didden and Schott 1992; Böning et al. 1991). One of the major deficiencies is the weakness of mesoscale fluctuations in middle and higher latitudes (Treguier 1991; Stammer and Böning 1992). The most plausible reason for the small intensity of the midlatitude eddy fields appears to be the rather coarse grid size used in the first CME runs, corresponding to a rather strong frictional control of the eddy generation.

In this paper, results from a sensitivity experiment directed at the effects of horizontal resolution/friction shall be reported. The experiment is based on the box model configuration of Cox, in the version with isotropic bottom roughness described by Böning (1989, hereafter B89). The "coarse"-grid (1/3° × 0.4°) experiment of B89 is repeated here with a finer grid size (1/6° × 0.2°) and appropriately reduced coefficients of horizontal friction. The sequence of experiments (Table 1) with this PE model in simplified geometry, driven by a steady wind stress and buoyancy flux, should provide a useful frame of reference for interpreting the solutions of geometrically more complex models with seasonally or daily varying forcing functions.

The outline of the paper is as follows. In section 2 a description of the numerical model is given. Comparison of the coarse- and fine-grid solutions begins with section 3 where the patterns of eddy energy are discussed. Section 4 deals with the generation mechanisms of eddy variability in different parts of the flow regime. The spatial structure of the eddies is discussed in section 5, based on wavenumber spectra and autocorrelation functions. The question of the role of the eddy variability for the meridional transport of heat is addressed in section 6, and conclusions are given in section 7.

2. Description of the numerical experiment

The experiment is based on the primitive equation, multilevel numerical model of Bryan (1969) in the version described by Cox (1984). The continuous equations of motion and continuity can be written as

$$\frac{\partial \mathbf{v}_h}{\partial t} + \mathcal{L}\mathbf{v}_h + w\frac{\partial \mathbf{v}_h}{\partial z} + \mathbf{f} \times \mathbf{v}_h = -\frac{1}{\rho_0}\nabla p + K_m \frac{\partial^2 \mathbf{v}_h}{\partial z^2} + \mathbf{F}_m \quad (1)$$

$$\frac{\partial p}{\partial z} = -\rho g \quad (2)$$

$$\nabla \cdot \mathbf{v}_h + \frac{\partial w}{\partial z} = 0. \quad (3)$$

Potential density ρ is a linear function of the single state variable T only, that is, $\rho = 1 - 2.5 \times 10^{-4}T$.

TABLE 1. Parameters of various eddy-resolving primitive equation models.

	Idealized geometry (Box)			Atlantic Ocean (CME)		World Ocean
	Cox (1985) C85	Böning (1989) B89	This study	Bryan and Holland (1989)	Böning et al. (1991)	Semtner and Chervin (1988)
Basin	Idealized: 0°–65°N, 0°–60° "E"			Atlantic: 15°S–65°N, 100°W–14°E		World Ocean
Bottom topography	flat	rough	rough	real topography		real topography
Grid size (meridional × zonal)	1/3° × 0.4°	1/3° × 0.4°	1/6° × 0.2°	1/3° × 0.4°		1/2° × 1/2°
Vertical levels	18	21	21	30		20
Number of grid points	197 × 152 × 18	197 × 152 × 21	393 × 303 × 21	240 × 220 × 30		720 × 280 × 20
Vertical						
diffusivity	0.3	0.3	0.3	0.3	0.3	
viscosity ($cm^2\ s^{-1}$)	10	10	10	30	10	
Horizontal						
diffusivity	2.4	2.4	0.4	2.5	2.5	7.5
viscosity [$(-1) \times 10^{19}\ cm^4\ s^{-1}$]	0.8	0.8	0.1	2.5	2.5	2.5

With $\rho = 1 + 10^{-3}\sigma$, the conservation equation for σ is

$$\frac{\partial \sigma}{\partial t} + \mathcal{L}\sigma + w\sigma_z = K_d \frac{\partial^2 \sigma}{\partial z^2} + F_d. \quad (4)$$

The ∇ operator and the nonlinear advection operator $\mathcal{L}$ apply to horizontal variations only; $\mathbf{v}_h$ is the vector of horizontal velocity, with components (u, v). The terms in F represent the effects of lateral turbulent mixing, given in biharmonic form,

$$\mathbf{F}_m = -A_m \nabla^4 \mathbf{v}, \quad F_d = -A_d \nabla^4 \sigma. \quad (5)$$

Here A_m, A_d are the horizontal and K_m, K_d are the vertical mixing coefficients corresponding to m: momentum, d: density. Convection is incorporated into the model through the convective adjustment procedure described in Bryan (1969).

The model ocean is forced by a steady zonal wind stress τ and by a surface buoyancy flux proportional to the deviation of the current surface density σ from a reference density σ^*. Both σ^* and τ are functions of latitude only and are shown in Fig. 1a.

In C85 the model was applied to a basin of 60° longitudinal width, extending from the equator to 65°N (Fig. 1b). Following a spinup phase of 540 years with a coarser, noneddy-resolving grid (1° × 1.2°), which resulted in a near steady-state solution, the 1/3° × 0.4° case was initialized and integrated another 24 years. In C85 a flat bottom was used, except for an idealized coast and shelf along the western wall. In B89 an idealized bottom topography, with a specified isotropic spectrum, was incorporated in the interior of the basin. In order to allow the representation of the topographically induced small flow scales on the numerical grid, the topographic spectrum was truncated at twice the smallest wavelength representable by the numerical grid. Interaction of the eddies with the bottom roughness reduced the strong barotropization tendency found in the flat-bottom case and led to more realistic vertical profiles of eddy kinetic energy (EKE). The present high-resolution experiment was initialized with the final density field of the rough-bottom case of B89, linearly interpolated to the new grid; initial velocities were set to zero. The truncation of the topographic spectrum was kept the same; that is, it is now four times the smallest wavelength. With the new grid size of 1/6° × 0.2° the model was integrated for 6 years.

In Table 1 the grid sizes and mixing coefficients used in the different versions of the box model are compared with the corresponding numbers used for the first experiments with the CME model of the North Atlantic. Also listed are the numbers used in the semiprognostic World Ocean model of Semtner and Chervin (1988). For the present fine-grid experiment with the box model, the same number of vertical levels (21) and the same vertical mixing coefficients (K_m = 10 cm^2 s^{-1}, K_d = 0.3 cm^2 s^{-1}) were used as in the coarser-grid case of B89. The horizontal mixing coefficients of the coarse-grid case,

$$A_m = -0.8 \times 10^{19}, \quad A_d = -2.4 \times 10^{19} \text{ cm}^4 \text{ s}^{-1}$$

were reduced to

$$A_m = -0.1 \times 10^{19}, \quad A_d = -0.4 \times 10^{19} \text{ cm}^4 \text{ s}^{-1}$$

in the fine-grid case. As may be seen in Table 1, the same horizontal grid size and similar horizontal mixing

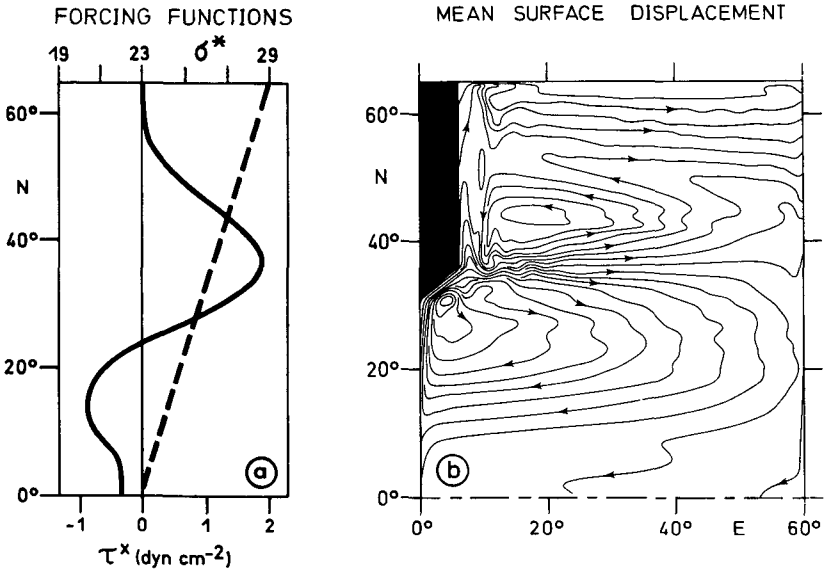

FIG. 1. The idealized model configuration of Cox (1985): (a) Zonal wind stress (solid line) and reference density (dashed line) at the surface, (b) 5-yr mean equivalent surface elevation of the coarse-grid (1/3° × 0.4°) model with contour interval = 10 cm.

coefficients as in the coarse-grid box experiments had been adopted for the CME North Atlantic model. The time step of 43.8 min used in the coarse-grid box was reduced to 21.9 min for the fine-grid case.

The integration period of 6 years with the high-resolution model is certainly not sufficient to allow the large-scale features of the deep ocean circulation to readjust to altered dynamics of the upper ocean due to the emergence of smaller flow scales. The main focus of this study is on the upper-layer flow, and on the nature of the eddy field in the solutions which react on a much shorter time scale. An indication of the adjustment process after initialization of the fine-grid case is provided by the temporal change of the basin-averaged kinetic energy (Fig. 2). After about 1 year of integration with the fine grid, a new, mean level of kinetic energy is reached that exceeds the energy of the coarse-grid solution by about 50%. As noted by Cox (1987) and B89 for the coarse-grid case, the kinetic energy is not constant even after a longer integration time; instead, a vacillation between kinetic and potential energy occurs, on a time scale of O(3 yr). In general, the presence of such low-frequency oscillations in the solution somewhat obscures a quantitative analysis of mean energy budgets over a certain period of time. For the purpose of this study, however, it is reasonable to assume that effects of these low-frequency fluctuations, for example, on EKE, are small compared to the effects caused by the different grid size.

In the following section the flow fields and eddy fluxes from the final 5 years of the fine-grid experiment will be compared with the coarse-grid solution of B89.

3. Eddy energy

The mean flow in the basin can be understood in terms of a meridional overturning cell driven by the differential buoyancy flux at the surface, superimposed by a wind-driven double gyre pattern with concentrated outflow at about 35°N. The surface geostrophic flow field, given in Fig. 1b, crudely approximates the main characteristics of midlatitude ocean circulation. The model is not intended as a simulation of a real ocean, however. Though basin dimensions are similar to those of the North Atlantic, significant deviations from a realistic flow pattern cannot be avoided with the simple geometry and the idealized forcing functions. In particular, the actual nonzonal course of the zero wind-stress curl line is not represented by the purely zonal wind stress used in the model. As outlined by C85, the peak in westerlies had been moved to 35°N, corresponding to the latitude of zero curl in the western North Atlantic. The independence of longitude causes a nearly zonal boundary between the subtropical and subpolar gyre, probably more representative of North Pacific than of North Atlantic conditions. These idealizations have to be kept in mind when interpreting the patterns of eddy variability occurring in the model.

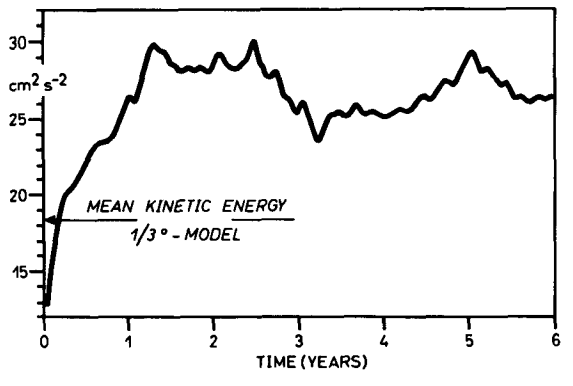

FIG. 2. Basin integrated kinetic energy vs integration time of the fine-grid (1/6° × 0.2°) model. The model was initialized with the final density field of the coarse-grid (1/3° × 0.4°) case; the mean energy of the coarse-grid solution is indicated.

Linear theory requires a changing sign of the meridional gradient of potential vorticity q as a necessary condition for baroclinic instability (Green 1960; Charney and Stern 1962). A northward decrease in q has been found as a striking feature of the upper thermocline ($\sigma = 26.3 - 26.5$) on the equatorward side of the subtropical gyre in the North Atlantic (McDowell et al. 1982). Since deeper layers are generally characterized by a northward increase in q, a large region in the North Atlantic, between 10° and 30°N, is potentially susceptible to baroclinic instability. The strongest reversal of the potential vorticity gradient is associated with the North Equatorial Current (NEC) at 12°–18°N, in 200–350 m. The NEC was suggested by Gill et al. (1974) as a potential region for baroclinic generation of eddies; the stability of this region was discussed by Keffer (1983). The time-mean density stratification and potential vorticity in the central/eastern part of the model basin is illustrated in Fig. 3a,b where meridional sections between 5° and 60°N are shown for the two box cases. Also shown (Fig. 3c) are the 5-yr mean fields of σ and q in the winter season of the WOCE Atlantic model. Potential vorticity is defined as $q = -(\zeta + f)\sigma_z$, where ζ is the relative vorticity of the flow. The general pattern of q is basically similar in all solutions. The ventilated portion of the subtropical gyre is characterized by a minimum of q, extending downward and southward from the convection areas in the northern portion of the gyre. This tongue of low q water separates two maxima of q associated with the main subtropical thermocline and with the shallow tropical thermocline and leads to a southward gradient of q in the upper layer of the subtropical gyre.

There are no significant differences between the stratification patterns of the coarse- and fine-grid solutions of the box model. However, there is only a rough correspondence to the solution of the Atlantic model. The meridional displacement of the wind forcing function and the idealization of the surface buoyancy fluxes cause a distortion of the stratification pat-

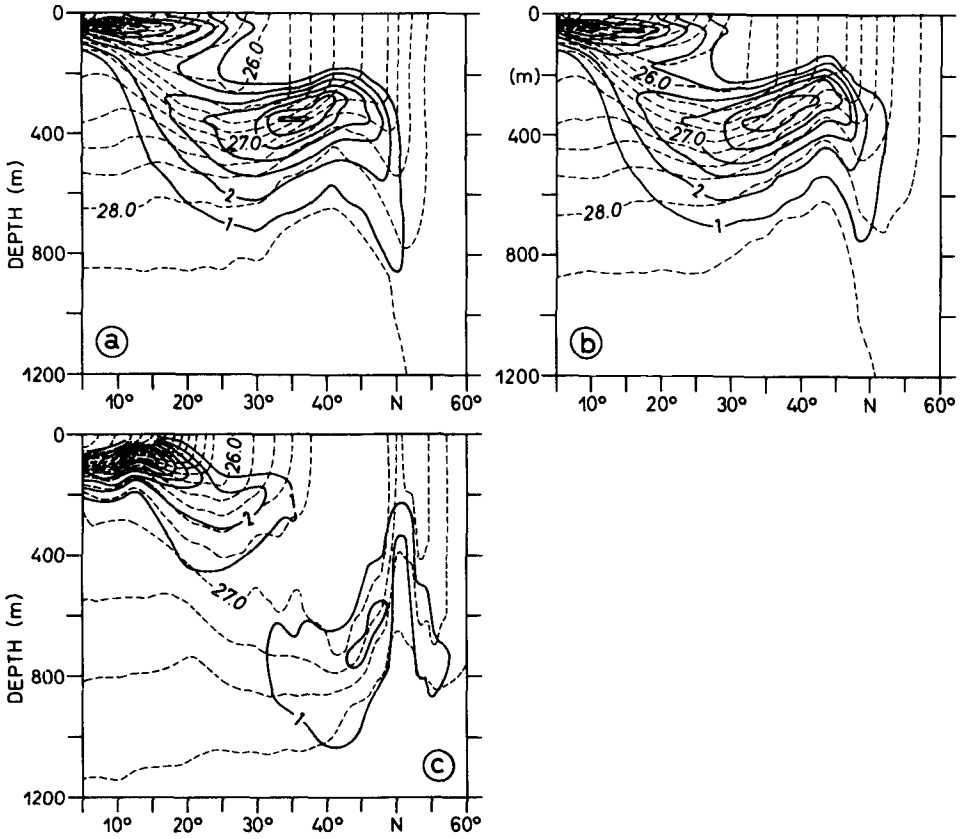

FIG. 3. Time-mean density and potential vorticity for (a) the coarse-grid case, (b) the fine-grid case of the box model, both averaged between 40° and 50°E; (c) the Atlantic model, averaged between longitudes 30° and 40°W. Solid lines represent q in units of 10^{-9} cm^{-1} s^{-1}, dashed lines represent σ in intervals of 0.2 sigma units.

tern in the box models, such as a much shallower thermocline than in the Atlantic case. It is obvious that these differences are of significance to the Charney–Stern conditions for baroclinic instability, which should caution against a quantitative comparison of the box results with observations.

The pattern of eddy kinetic energy density (EKE) at the surface of the box is given in Fig. 4a,b for the coarse- and the fine-grid case. Highest eddy variability is associated with the central jet at about 35°N. Very weak energies are found in the eastern part of the basin between 30° and 45°N. A band of moderate eddy activity extends across the basin along the westward-flowing portion of the subtropical gyre, between 15° and 20°N. In the fine-grid case, nearly the whole basin has become more energetic. Over the subtropical gyre, EKE is roughly twice as high as in the coarse-grid case: more than 2000 cm^2 s^{-2} are obtained in the jet area, and 200 cm^2 s^{-2} are reached at the southeastern flank of the gyre. New instability areas seem to be emerging in the northern part of the basin, where variability was rather weak in the coarse-grid case.

There are at least two main departures from the eddy variability pattern obtained with the CME model (Treguier 1991; Stammer and Böning 1992) that have to be related to the distortions of the basin and forcing geometries mentioned above. In the box models there are no counterparts for the high-energy densities along the North Atlantic Current that exceed 600 cm^2 s^{-2} east of Newfoundland, at 50°N (Krauss and Käse 1984). On the other hand, eddy intensities in the North Equatorial Current (NEC) are much larger than both the values obtained in the CME and the values suggested by current measurements (Fu et al. 1982). However, while the box model values of EKE in the subtropics are probably exaggerated due to the distorted forcing geometry, the pattern of eddy variability, with a minimum in the center of the subtropical gyre and an increased energy level along the westward-flowing portion of the gyre, does not appear inconsistent with existing data. An increase of eddy activity into the NEC, from a broad zonal minimum between 24° and 30°N, is shown by the maps of temperature variance and eddy potential energy that were obtained from expendable bathythermograph records by Dantzler (1977) and Emery (1983).

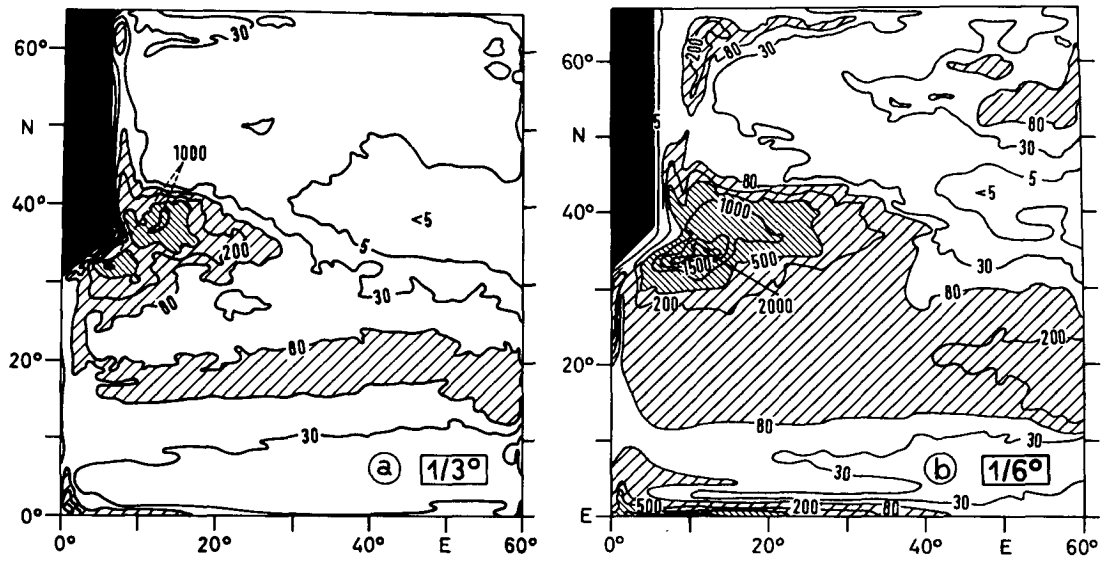

FIG. 4. Eddy kinetic energy in units of $cm^2\ s^{-2}$ at the surface for (a) the coarse-grid case and (b) the fine-grid case.

Another perspective of the distribution of eddy variability and its sensitivity to the horizontal grid size is given in Fig. 5, where meridional sections of eddy kinetic energy and temperature standard deviation, $T_{rms} = \overline{T'T'}^{1/2}$, are shown for zonal averages between 40° and 50°E. The section through the eastern part of the basin is the same as that used for the potential vorticity section of Fig. 3. Two areas of intensified eddy variability are revealed: the larger one in the southern portion of the subtropical thermocline where the saddle-shaped pattern of q indicated favorable conditions for baroclinic instability, and a weaker maximum in the subpolar area, centered at about 50°–55°N. (As may be seen in the horizontal map of Fig. 4, another band of intense eddy activity occurs near the equator. It will not be examined further here, since the flow behavior is probably influenced very much by the presence of the southern wall.)

With the finer grid the maximum EKE in the subtropical thermocline becomes roughly twice as large as in the coarse-grid case. Surface EKE in the subpolar region increases by a factor of 4. In both cases these areas of moderate eddy activity are separated by a zone of very weak energy, roughly associated with the region of broad eastward flow at about 40°N. The latitude ranges of enhanced EKE correspond to enhanced values of rms temperature. South of 25°N, a shallow maximum of T_{rms} is associated with the tropical thermocline; another broad maximum occurs in the main thermocline between 15° and 30°N, with highest values at depths of 400–500 m. The temperature standard deviations found in the model zone from 15° to 30°N, between 0.5° and 1.0°C, are in rough agreement with the values given by Emery for the zonal bands of enhanced eddy activity in the subtropical North Atlantic (between 15° and 22°N) and the North Pacific (between 20° and 30°N).

An interesting feature of the eddy variability patterns is the different sensitivity of EKE and T_{rms} to the horizontal grid resolution and friction. This situation is exemplified in Fig. 6, where mean vertical profiles of EKE and eddy available potential energy (EPE) are shown for 10° × 10° regions in the subtropical and subpolar eddy fields. Eddy potential energy is related to the temperature variance, normalized by the stability of a mean reference state [see section 4, Eq. (10)]. While EKE decreases with increasing depth through the main thermocline, maximum values of temperature variance, and, accordingly, EPE are found at subsurface levels. In general, this model feature reflects the observed pattern; for example, the POLYMODE moorings in the NEC at 16°N indicated local maxima of EPE above 200 m and between 320–540 m (Fu et al. 1982). However, the most important point to note in the box model solutions is probably the different change of EKE and EPE between the coarse- and fine-grid case. Especially in the subpolar area, temperature variance and EPE appear as much more robust model quantities than EKE. The different changes of EKE and EPE when going from coarse to fine resolution imply different ratios of EKE to EPE in the two solutions. As will be discussed below, this is consistent with a decrease of the energetic eddy scales in the fine-grid case.

While the generation of eddy variability in the eastern part of the basin, as will be shown in section 4, can be understood in terms of a baroclinic instability mechanism, the influence of the Reynolds stresses is not negligible in the strong shear zones associated with

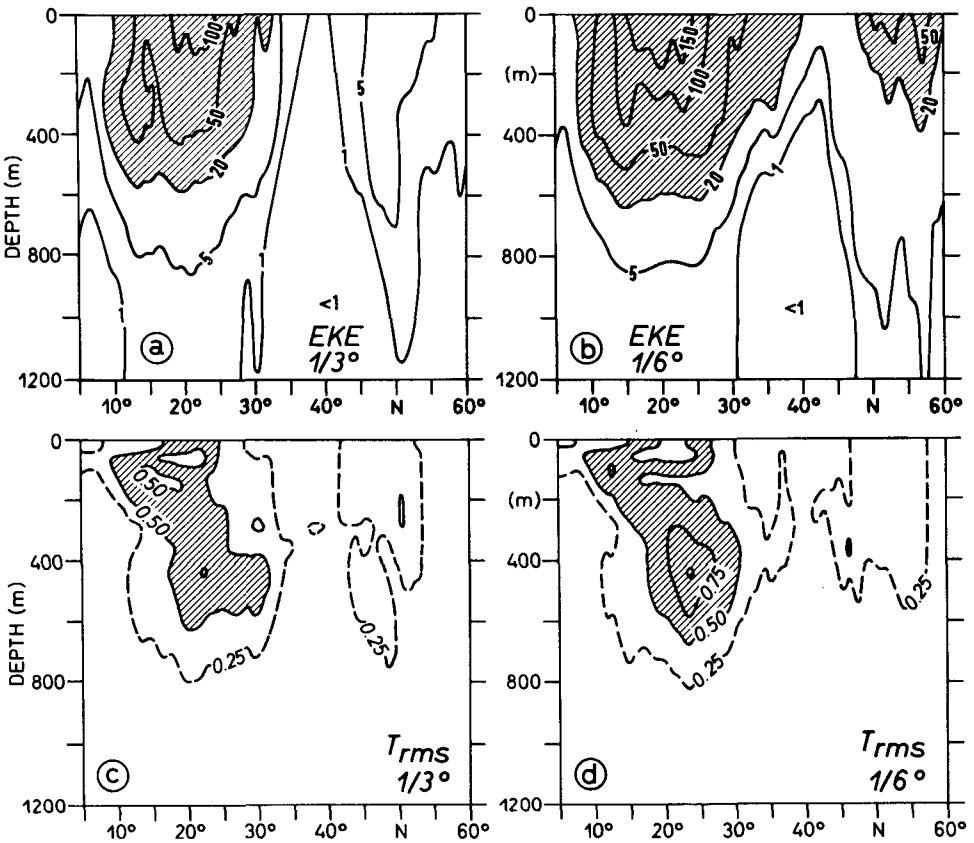

FIG. 5. Eddy kinetic energy (in units of $cm^2\ s^{-2}$) for (a) the coarse- and (b) the fine-grid case; and standard deviation of temperature (in °C) for (c) the coarse- and (d) the fine-grid case. Quantities are averaged between 40° and 50°E.

the central eastward jet. Meridional sections through the energetic jet regime are given in Fig. 7 showing the mean density, potential vorticity, eddy kinetic energy, and temperature variance for zonal averages between 10° and 20°E. There seem to be only small differences in the density structure of the coarse- and fine-grid solutions. The 350–400-m deep part of the density front is associated with a pronounced maximum of potential vorticity; below this maximum, gradients of q are very weak along the isopycnals. The q pattern implies that favorable conditions for baroclinic instability should occur in a zonal strip centered at about 34°–36°N. The difference in eddy variability between the two solutions is stronger than in the eastern part of the basin: the maximum temperature variance of 6 $(°C)^2$ in the coarse-grid case increases to 9 $(°C)^2$ in the fine-grid case; correspondingly, the maximum values of EPE in the front increase from 5000 to 8000 $cm^2\ s^{-2}$. A difference of more than a factor of 2 in this zonal average is obtained for the EKE maximum: at the surface 600 $cm^2\ s^{-2}$ are found in the coarse- and 1300 $cm^2\ s^{-2}$ in the fine-grid case.

4. Eddy–mean flow interaction

In this section we shall seek information on the generation and the dynamical role of the time-variant (eddy) part of the flow by a consideration of the energy cycle in various regions. After giving some necessary definitions, energy budgets will be presented in the form of the box diagram introduced by Lorenz (1955) showing the energy transfer terms acting upon the various components of the total energy of the system.

The available potential energy participating in the energy cycle was defined by Lorenz as the difference between the total potential energy in the actual state and that of an isentropically leveled state. Though internal energy ($= \int\int\int \rho^* c_p T dV$, where ρ^* is the in situ density and c_p the specific heat at constant pressure) represents a large fraction of the total potential energy of the ocean (Oort et al. 1989), the available part of it appears negligible compared to the available gravitational potential energy (Reid et al. 1981). Under the usual assumption that horizontal gradients in density are much smaller than vertical gradients, the available

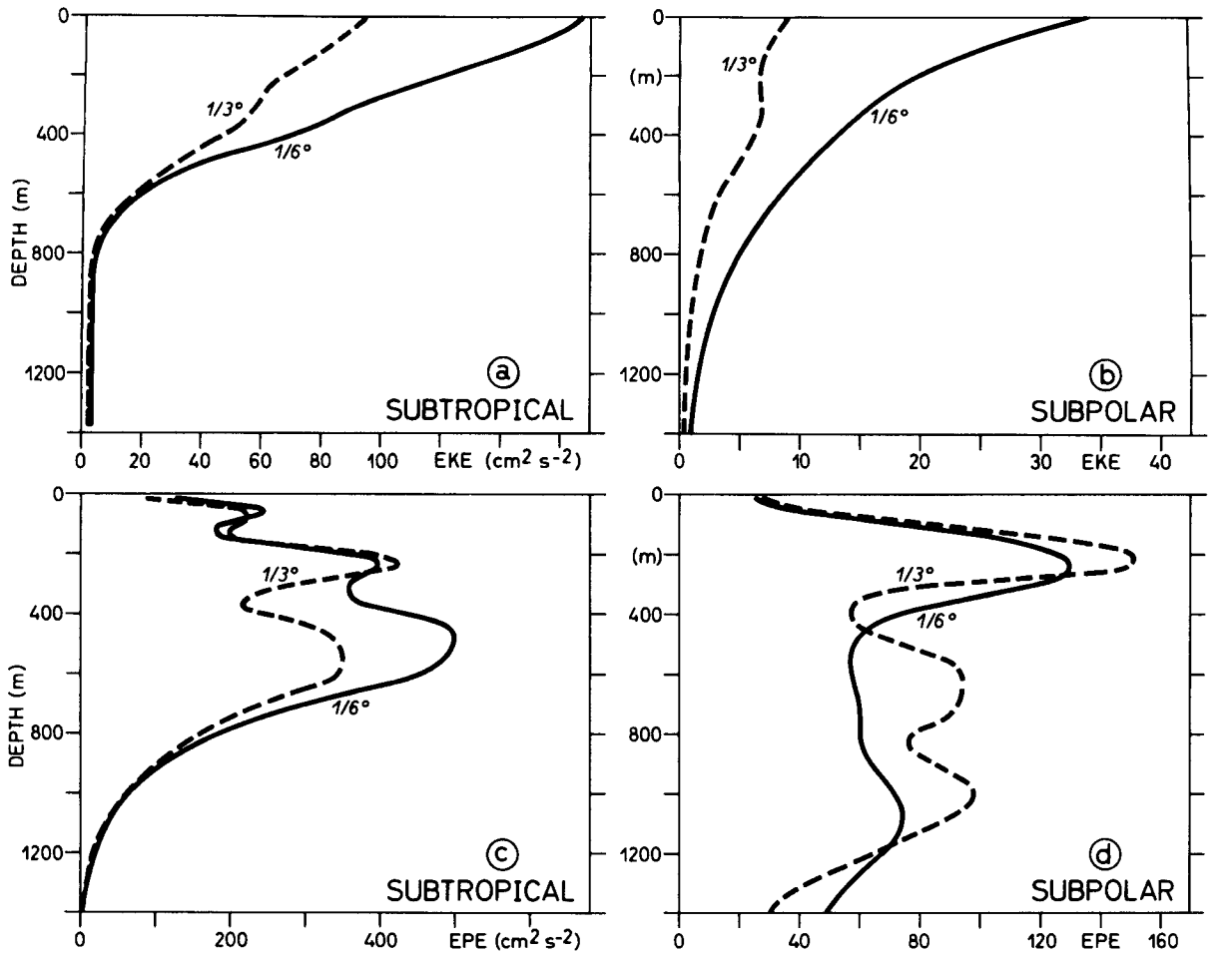

FIG. 6. Vertical profiles, averaged over 10° by 10° subregions, of eddy kinetic energy for (a) the subtropical and (b) the subpolar gyre; and eddy available potential energy for (c) the subtropical and (d) the subpolar gyre. Solid lines represent the fine-grid case, dashed lines the coarse-grid case.

potential energy per unit mass in a volume element V may then be approximated by (e.g., Oort et al. 1989)

$$P = -\frac{1}{2} g \iiint \frac{(\rho - \tilde{\rho})^2}{d\tilde{\rho}/dz} dV, \tag{6}$$

or, using the linear relation between potential density and potential temperature, $\rho = \rho_0(1 - \alpha T)$,

$$P = \frac{1}{2} \alpha g \iiint \frac{(T - \tilde{T})^2}{d\tilde{T}/dz} dV. \tag{7}$$

The reference state, $\tilde{\rho}(z)$, is obtained here as the horizontal average over the time-mean density distribution.

Neglecting the contribution of vertical velocity w, the kinetic energy per unit mass is given by

$$K = \frac{1}{2} \iiint (u^2 + v^2) dV. \tag{8}$$

Separating the actual flow variables into time mean and transient parts, $u = \bar{u} + u'$, etc., the time-mean energy of the system may be divided into four components:

mean available potential energy (PEM)

$$\frac{1}{2} g\alpha \iiint \frac{(\bar{T} - \tilde{T})^2}{d\tilde{T}/dz} dV, \tag{9}$$

eddy available potential energy (EPE)

$$\frac{1}{2} g\alpha \iiint \frac{\overline{T'^2}}{d\tilde{T}/dz} dV, \tag{10}$$

mean kinetic energy (KEM)

$$\frac{1}{2} \iiint (\bar{u}^2 + \bar{v}^2) dV, \tag{11}$$

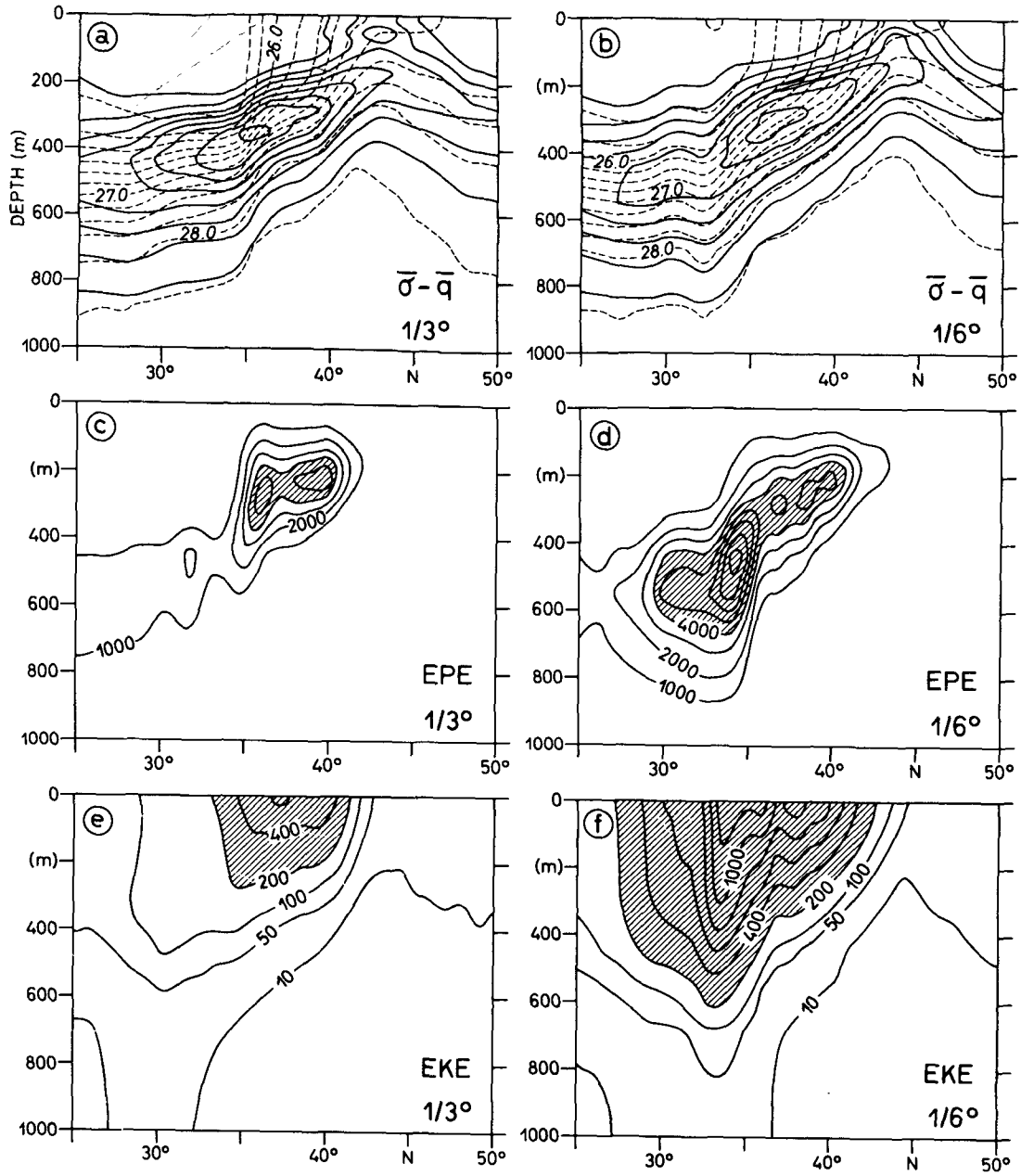

FIG. 7. Quantities averaged between 10° and 20°E, over the midlatitude jet regime. Density (dashed lines) in intervals of 0.2 sigma units, and potential vorticity (solid lines) in intervals of 10^{-9} cm^{-1} s^{-1} for (a) the coarse- and (b) the fine-grid case; eddy available potential energy in intervals of 1000 cm^2 s^{-2} for (c) the coarse- and (d) the fine-grid case; and eddy kinetic energy for (e) the coarse- and (f) the fine-grid case; interval is 200 cm^2 s^{-2} for values higher than 200 cm^2 s^{-2} (dashed area).

eddy kinetic energy (EKE)

$$\frac{1}{2}\int\int\int (\overline{u'^2 + v'^2})dV. \qquad (12)$$

If integrated over a closed domain, an energy component can change by the work of external forces on the system, that is, wind work (W) and buoyancy work (B), by diffusion (D) and frictional dissipation (F), or by energy transfers due to interactions with other components (T_i). The energy cycle in this case may be presented in the form of an energy box diagram, as shown in Fig. 8.

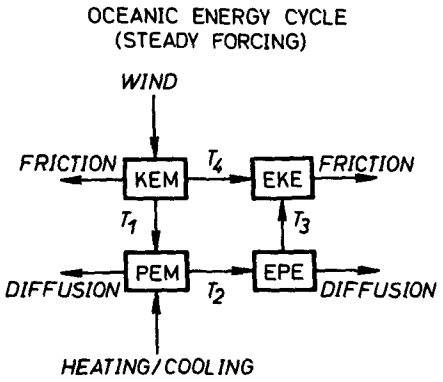

FIG. 8. Schematic diagram indicating the mean energy cycle for a closed oceanic basin, driven by steady wind and buoyancy forcing. Definitions for the energy components and energy transfers are given in the text.

The energy transfers, per unit mass, in a closed volume V are given by

$$T_1 = \alpha g \iiint \bar{w}\bar{T}\,dV \tag{13}$$

$$T_2 = \alpha g \iiint \frac{\overline{u'T'}\partial\bar{T}/\partial x + \overline{v'T'}\partial\bar{T}/\partial y}{d\bar{T}/dz}\,dV \tag{14}$$

$$T_3 = -\alpha g \iiint \overline{w'T'}\,dV \tag{15}$$

$$T_4 = -\iiint \left\{\overline{u'u'}\frac{\partial\bar{u}}{\partial x} + \overline{u'v'}\left(\frac{\partial\bar{v}}{\partial x} + \frac{\partial\bar{u}}{\partial y}\right) + \overline{v'v'}\frac{\partial\bar{v}}{\partial y}\right\} dV \tag{16}$$

where T_1 represents the conversion of mean kinetic to mean potential energy by the work of the mean buoyancy forces, T_2 the conversion of mean to eddy potential energy (baroclinic instability), T_3 the conversion from eddy potential to eddy kinetic energy, and T_4 the work of the Reynolds stresses against the mean shear (which, if positive, represents barotropic instability).

The situation becomes considerably more complex when energy budgets of subregions of a turbulent flow are considered. Energy in an arbitrary volume of fluid is enhanced also by transports of energy into the region due to mean flow and mean eddy advection and due to the divergence of mean and eddy pressure work. In addition, the Reynolds interaction work no longer represents a conversion of energy between KEM and EKE: that is, T_4 represents the effect of eddy–mean flow interaction on EKE, but not its effect on KEM. Kinetic energy budgets over various subregions of wind-driven model gyres have been examined by Harrison and Robinson (1978) and Hall (1986). Treguier (1991) computed kinetic energy balances for subregions of the CME Atlantic model and compared the results with previous QG models of idealized, wind-driven ocean basins.

A complete analysis of the energy cycle in open subregions is beyond the scope of the present study. The focus here shall be on the eddy generation mechanism and its dependence on grid resolution. Motivated by the eddy energy patterns as described in the previous section, three major flow regimes will be distinguished:

(i) the subpolar region, 40°–60°N, 25°–60°E,
(ii) the southern portion of the subtropical gyre, 10°–30°N, 25°–60°E, and
(iii) the central jet regime, 32°–38°N, 8°–25°E.

For each of these regions, the four components of energy and the four interaction terms, T_i, have been computed. The results for the central jet (iii), and the two "interior" regions (i), (ii) will be discussed separately, beginning with the latter.

For the purpose of an easier comparison, the numbers for the subpolar and subtropical gyre are displayed in Fig. 9 in the form of an energy budget as shown in Fig. 8. If we assume that the solution is near statistical equilibrium, the imbalance between each pair of interaction terms T_i represents the sum of all other energy fluxes into or out of the subregion. The so-defined energy cycle is illustrated in Fig. 9 by arrows whose widths characterize the strength of the particular flux term.

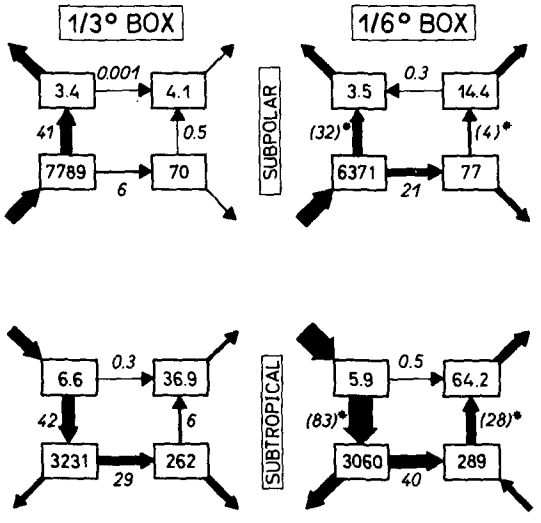

FIG. 9. Values of the energy components (in $cm^2\ s^{-2}$) and interaction terms (in $10^{-5}\ cm^2\ s^{-3}$) for two subregions of flow, *schematically* displayed in the form of an energy cycle diagram. The width of the arrows is proportional to the strength of the corresponding energy flux. The imbalance between each pair of interaction terms is indicated by a flux into or out of the corresponding energy box, and represents the net effect of forcing, dissipation, and energy transport across the boundaries of the subregion. (Values marked by an asterisk are strongly sensitive to the particular choice of the subregion.)

(It should be noted, however, that the meaning of the residual fluxes is different than in the basin-averaged diagram shown in Fig. 8 due to the presence of pressure work and advective fluxes.)

Two basically different types of the energy cycle can be distinguished in the model ocean. In the subtropical gyre the energy input is to KEM, balanced by a transfer of energy to PEM. This can be understood as the effect of the wind-driven gyre on the density stratification. It implies a net negative correlation between vertical motion and temperature over the gyre; that is, upward motion is associated with denser water and sinking motion with less dense water. The transfer from the pool of kinetic energy maintains the mean potential energy of the subtropical gyre against the work of the buoyancy forces; that is, mean heating at the surface and baroclinic instability. In general, wind-driven QG oceans are controlled by a similar type of energy cycle (with widely varying ratios of baroclinic to barotropic instability transfers). The dynamics of the subpolar area is characterized by a fundamentally different energy cycle. The main energy input is to PEM (most plausibly interpreted as the effect of the buoyancy fluxes at the surface). Kinetic energy is generated mainly by a conversion of potential energy associated with the downward motion of denser water, and not by wind work. Apparently, there can be no counterpart of such an energy cycle in wind-driven, adiabatic QG models.

In both flow regimes, eddy energy is generated primarily by conversion from mean potential energy, that is, by baroclinic instability, and interaction between KEM and EKE is negligible. Everywhere in the basin the transfers between mean potential and eddy potential energy take a much stronger role in the mean energy balance when going from the coarse to the fine grid. This is especially the case in the subpolar region, where the interaction with eddies appears of rather minor importance for the mean energetics in the coarse-grid solution: the loss of PEM by the baroclinic instability processes is only 14% of the energy conversion to KEM. In this area, doubling the resolution enhances the baroclinic instability transfer by a factor of 3.5. The corresponding factor is 1.4 for the subtropical gyre, and, as shown later, 3.2 for the central jet. These values roughly correspond to the increase of EKE from the coarse- to the fine-grid solution: 3.5 in the subpolar, 3.8 in the jet, and 1.7 in the subtropical region. It should be noted that all values depend to some degree on the actual choice of the subregion. This is especially the case for the buoyancy work terms, T_1 and T_3, which have a rather noisy spatial dependency. [Transfer terms marked by an asterisk (*) should therefore be interpreted in a qualitative way only.]

As noted in the previous section, the potential energy of the transients is much less sensitive to grid resolution than the kinetic energy, except for the jet area. In the subpolar and the subtropical region there is roughly a 10% increase of EPE, and a decrease of PEM by a similar percentage. Theoretically, the ratio of available potential to kinetic energy should correspond to $(L/L_D)^2$, where L is the scale of the flow and L_D the radius of deformation (e.g., Pedlosky 1979). The energy ratios, $(\mathrm{PEM/KEM})^{1/2}$ and $(\mathrm{EPE/EKE})^{1/2}$, are evaluated in Table 2 for the coarse- and the fine-grid case. In all regions, the change of eddy energy corresponds to a decrease of the eddy scale relative to the deformation radius. The change of the eddy scale between the coarse- and the fine-grid case is smallest in the subtropical gyre, and strongest (L decreases by a factor of 2) in the subpolar region. It is interesting to note that in the fine-grid case the scale ratio is nearly constant throughout the basin. Changes in the mean energy ratios are rather small. The available potential energy stored in the subtropical gyre exceeds the kinetic energy of the mean flow by a factor of 500. Gill et al. (1974) estimated an energy ratio of O(1000) for the subtropical North Atlantic.

Box diagrams appear as a less useful means of characterizing the energy cycle in the region of the central jet because of a much stronger spatial variability of the energy transfer terms than in interior of the basin. The meridional structure over the jet axis of the baroclinic and barotropic transfer terms, T_2 and T_4, is illustrated in Fig. 10, in relation to the pattern of KEM and EKE. The meridional profiles represent averages between 10° and 20° longitude, and over the top 980 m of the jet. Some caution should be executed in interpreting these profiles, since there is variability also along the jet. Although the zonal structure appears generally weaker than the cross-jet variation, it implies that a zonal-mean profile is not quantitatively representative of any individual section, and depends to some degree on the extent of the zonal-averaging interval. Both effects contribute to the mean energy profiles displayed in Fig. 10. Due to the presence of permanent meanders in the mean field, the zonally averaged mean jet is less sharp than at individual sections; the meridional displacement of the jet axis is partly an effect of the particular averaging interval, which cuts the meanders of the coarse- and fine-grid solution at a somewhat different

TABLE 2. Ratio of mean eddy available potential to mean eddy kinetic energy in different subregions for the coarse- and fine-grid case. (The values for the mean energy ratio in the central jet, marked by an asterisk, are strongly dependent on the meridional extent of the averaging area.)

	$(\mathrm{PEM/KEM})^{1/2}$		$(\mathrm{EPE/EKE})^{1/2}$	
	Coarse grid	Fine grid	Coarse grid	Fine grid
Subpolar	47.6	42.4	4.1	2.3
Central jet	7.7*	8.5*	3.0	2.4
Subtropical	22.1	22.7	2.7	2.1

TABLE 3. Kinetic energy densities (in $cm^2 s^{-2}$) of mean flow (KEM) and eddies (EKE), and energy transfer terms (in 10^{-4} $cm^2 s^{-3}$), T_2 (baroclinic instability), and T_4 (barotropic instability), for the central jet region. The values are obtained by averaging over the depth range 0–980 m, the zonal interval 10°–20°E, and the latitudes 33°L–38°N (for the coarse-grid case), 31°–36°N (fine-grid case).

	Coarse grid	Fine grid
KEM	103	150
EKE	135	518
T_2	1.8	5.8
T_4	0.2	−0.4

phase. Apart from this apparent southward displacement, the mean jet in the fine-grid case shows a similar structure to that in the coarse-grid solution; integrated over the region the mean kinetic energy increases by about 50% (Table 3). In contrast, the kinetic energy of the eddies averaged over the same interval increases by a factor of 3.8.

Probably the most prominent feature of the sections is the strong difference between the energy transfer terms of the two solutions. In the coarse-grid case, the barotropic interaction term T_2 appears generally negligible compared to the baroclinic transfer T_4. As may be seen also in Table 3, the baroclinic transfer remains the dominant source of eddy variability in the fine-grid case; the section average of T_2 increases by a factor of 3.2, roughly corresponding to the increase of EKE. An inspection of vertical sections shows that nearly all of this conversion between mean and eddy potential energy takes place in the upper 400 m. An even stronger tendency is shown by the barotropic interaction term T_4, which increases by an order of magnitude in the fine-grid case. Particularly interesting is the meridional structure of this term. The large negative values near the jet axis correspond to an energy loss of the eddies by the Reynolds interaction work. Though the interaction term T_4, as noted above, in an open subregion of flow does not exactly represent the effect of the fluctuations on the mean flow, the pattern suggests that the eddies act to maintain the mean shear of the flow. Due to the sign reversals in the meridional direction, the net section-averaged value of the fine-grid solution

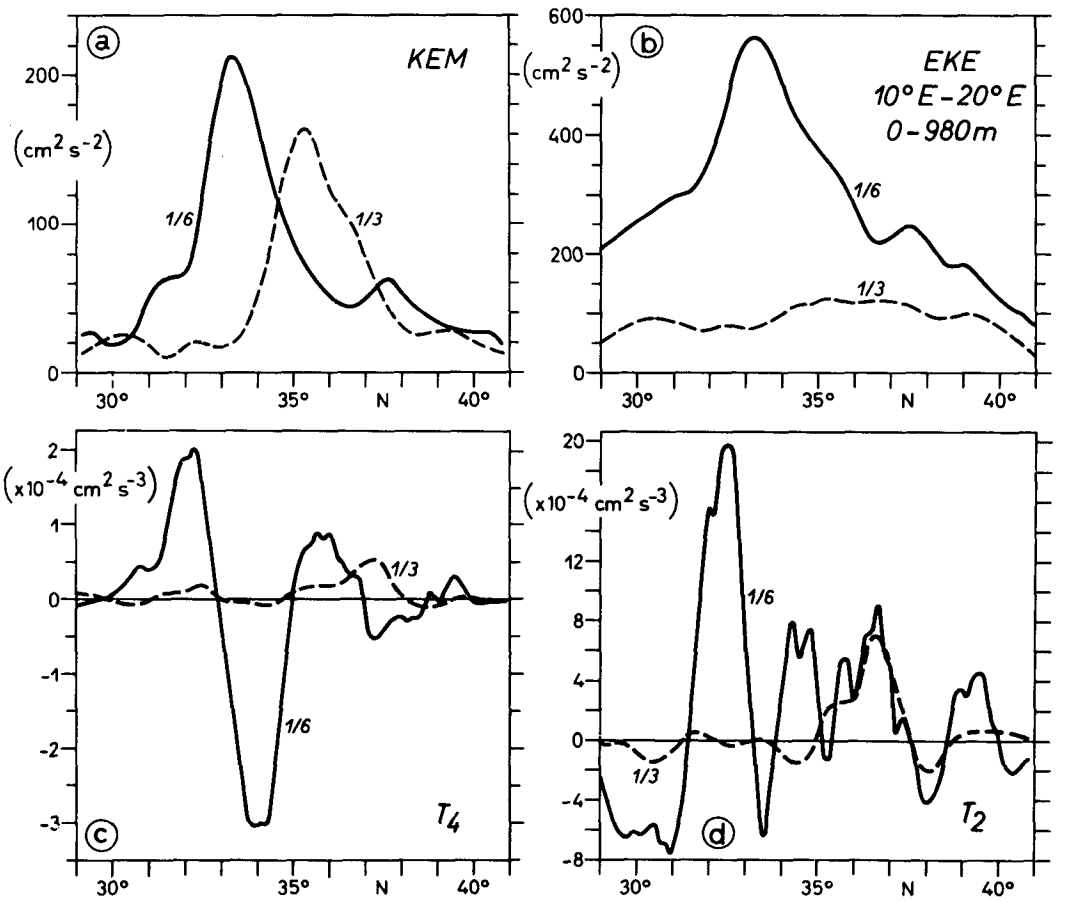

FIG. 10. Energetics of the midlatitude jet: (a) kinetic energy of the mean flow, (b) eddy kinetic energy, (c) barotropic instability, and (d) baroclinic instability. Quantities are averaged between 10° and 20°E, and 0–980 m.

as shown in Table 3 does not express the strong difference to the coarse-grid case.

The interaction work T_4 comprises the work of the Reynolds stresses against the gradients of the mean flow in both along- and cross-stream directions. Due to the presence of quasi-stationary meanders of the (nearly) zonal jet, there is a contribution from all three terms $\overline{u'u'}\,\partial\bar{u}/\partial x$, $\overline{v'v'}\,\partial\bar{v}/\partial y$, and $\overline{u'v'}\,\partial\bar{u}/\partial y$, respectively. The structure of the latter term in the fine grid is illustrated in Fig. 11 showing a latitude–depth section of the momentum flux $\overline{u'v'}$, superimposed on the $\bar{u}$ = 20 cm s^{-1} isotach. In contrast to the coarse-grid case (not shown), where the momentum flux is very weak and less organized, there is a systematic pattern with a strong northward flux of zonal momentum south of the jet axis, and vice versa. Even in this zonally averaged section, the extrema at both sides of the jet are about ± 150 cm^2 s^{-2}.

A basically similar pattern of a zonal momentum flux convergence was indicated by field investigations in the Gulf Stream and Kuroshio Extension. The current meter results of Schmitz (1977), along 55°W and 70°W, suggested a tendency of the off-diagonal Reynolds stress component to intensify the mean Gulf Stream. A similar pattern, with positive values of $\overline{u'v'}$ south and negative values north of the jet axis, was found over the Kuroshio Extension, based on XBT data (Nishida and White 1982), current meter results (Schmitz et al. 1982), and Geosat altimeter data (Tai and White 1990).

The direction of the eddy momentum flux in baroclinic instability had been investigated by Held and Andrews (1983). Their perturbation theory indicated that the momentum flux tends to be into the jet if the scale of the horizontal shear is not smaller than the radius of deformation. Results from QG experiments with a limited number of vertical layers have generally been found highly dependent on parameter choices and showed either barotropic, baroclinic, or mixed instabilities of the midlatitude jet (Holland et al. 1983). An idealized PE model of the meandering Gulf Stream by Wood (1988) showed baroclinic instability as the predominant energy source for the transients, and a tendency for the momentum flux to reinforce the mean jet. The present results suggest that the PE model begins to simulate this characteristic pattern of the horizontal eddy fluxes near open-ocean jets, provided the grid resolution, as in the 1/6° case, is high enough.

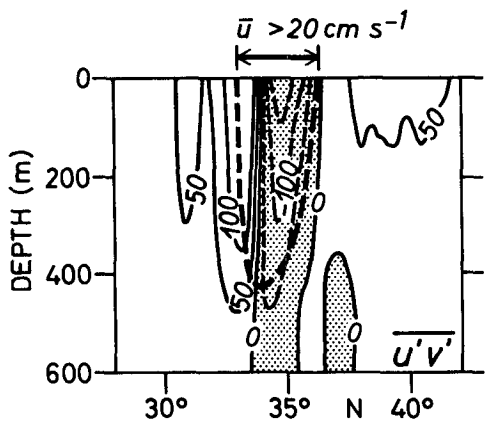

FIG. 11. The off-diagonal component of the Reynolds stress tensor, $\overline{u'v'}$, for the fine-grid case; averaged between 10° and 20°E. Contour interval is 50 cm^2 s^{-2}, stippling denotes negative values. The heavy dashed line represents the 20 cm s^{-1} isotach of the mean zonal flow.

Whether there is a net impact of the altered eddy dynamics on the downstream structure of the jet is examined in Fig. 12. It shows the zonal variation of the mean and eddy kinetic energy, averaged between 31° and 38°N, and over the upper 980 m. Probably the most interesting feature here is the rather small difference between the zonal penetration scale of the 1/3° and 1/6° model jets, despite their strongly different eddy intensities. The mean flow in the fine-grid case is intensified between 9° and 15° east of the western boundary; beyond that there is no significant difference. A similar insensitivity of the mean jet had been obtained when bottom roughness was incorporated in the originally flat-bottomed C85 model (B89). While this had a strong influence on the vertical structure of EKE, effects on the mean flow were negligible. The rather robust nature of the mean jet in the PE solutions stands in contrast to model results based on the QG approximation. The zonal jet scale of QG models has generally been found very sensitive to various model parameters (Holland and Schmitz 1985). A 6-layer model forced by a symmetrical (double-gyre) wind stress showed a 40% increase of the central jet's penetration scale when the grid spacing was reduced from 20 to 10 km (Barnier et al. 1991). Whether the insensitivity of the PE jet to the strongly enhanced eddy field is a special result of the particular model configuration used here has to remain open. It is interesting to note, however, that a similar insensitivity is shown by the mean heat transport across the jet (see section 6); both features would have to be expected as a consequence of the "nonacceleration theorem" (Andrews and McIntyre 1976).

5. Spatial scales

In this section the spatial characteristics of the eddy field, as simulated by the different model grids, shall be examined. Snapshots of the instantaneous flow in different model regions are given in Fig. 13, for the fine-grid solution. The meandering jet sheds and interacts with eddies of about 250 km diameter (Fig. 13a). Ringlike vortices also characterize the flow field in the interior of the subtropical gyre (Fig. 13b). An

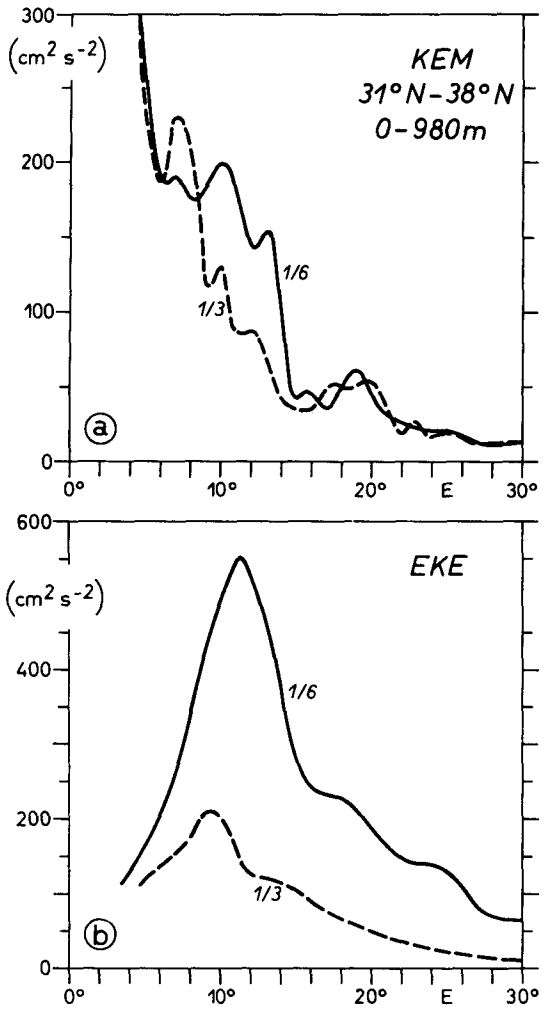

FIG. 12. Zonal variation of (a) mean flow and (b) eddy kinetic energy in the central jet regime, averaged between 31° and 38°N, and 0–980 m depth.

analysis of the space–time structure of the model solution in B89 showed a pronounced tendency of the fluctuations in the subtropical thermocline to become concentrated in singular energetic structures, propagating westward with typical phase speeds of 6 cm s^{-1}. In particular, the anticyclonic eddies appeared very stable and generally retained their identity for a year or more. In contrast to the ringlike structures of the jet regime and in the subtropical gyre, the velocity fluctuations in the subpolar model area appear much less organized, and are of substantially smaller scale (Fig. 13c).

In order to allow a comparison between the spatial characteristics of the coarse- and fine-grid solutions, one-dimensional wavenumber spectra were calculated from more than 50 individual realizations of the instantaneous velocity field during the last 5 years of each experiment. In an attempt to avoid effects of statistical inhomogeneity, which are especially obvious in the meridional direction, spectra were estimated along zonal sections over the interior of the basin only, and

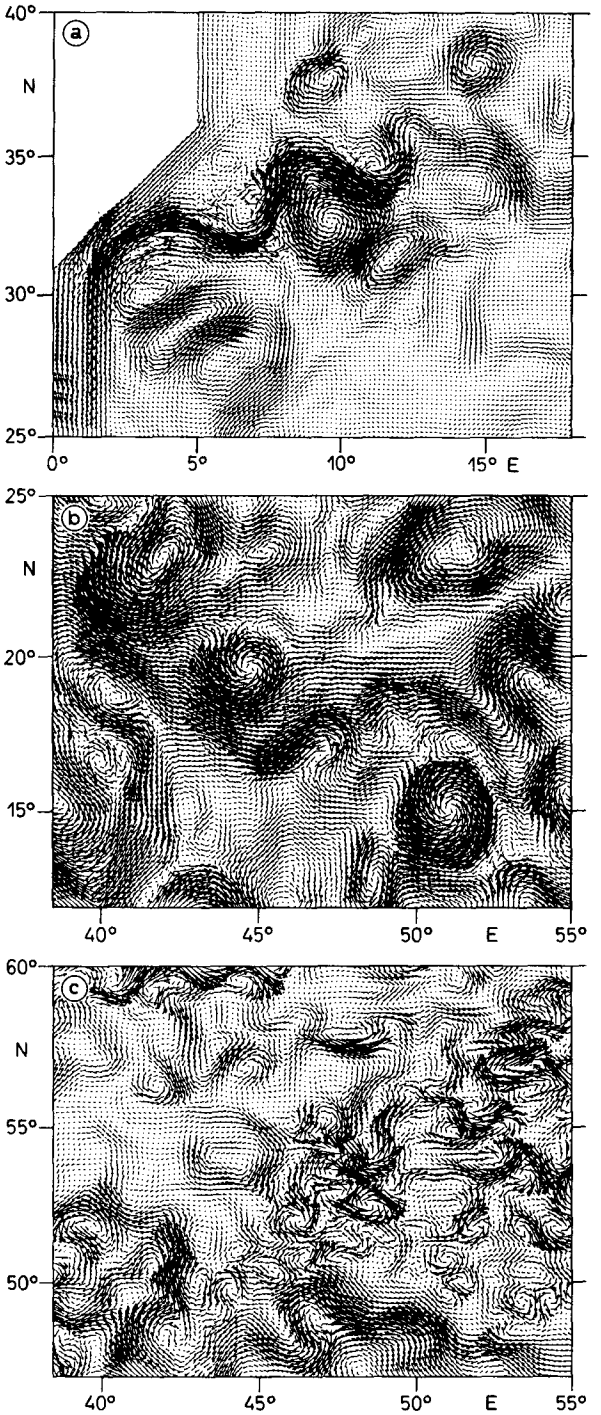

FIG. 13. Maps of instantaneous flow fields in the fine-grid model: (a) central jet regime, (b) subtropical gyre, (c) a subpolar region.

averaged over certain latitude bands. Zonal variation of flow statistics is especially weak in the subtropics, and it may be acceptable in parts of the subpolar area. Accordingly, spectra will be presented for the latitudinal bands 12°–24°N, 24°–30°N, and 52°–60°N. Since it is difficult to find any statistically homogeneous subregion significantly exceeding the eddy scale in the regime of the central jet, this area was omitted from the spectral analysis. Instead, and to provide a contrast to the characteristics of the turbulent eddy field in midlatitudes, spectra are presented for the near-equatorial fluctuations in the tropical band 2.5°–5.5°N. No spectral smoothing was applied, except for averaging the individual zonal spectra over the latitude ranges, and over the ensemble of realizations.

Figure 14 depicts the zonal wavenumber spectra characterizing the surface velocity field of both model cases. In general, all regions exhibit red spectra beyond a certain cutoff wavenumber; the corresponding wavelength, indicated at the top of each frame, decreases with latitude. The near equatorial region appears distinct from the others with a much steeper spectral slope; the fluctuations in this region are apparently of a largely monochromatic nature. In this tropical band a difference between the model solutions is confined to the energy density near the preferred wavelength of about 770 km, which becomes significantly more excited in the fine-grid case. Influences on higher wavenumbers are obviously negligible, except for the smallest scales resolved by the model grids. (In contrast to the extratropical regions, the scale-selective friction mechanism seems barely effective enough here to control the grid-scale noise, especially in the coarse-grid model. This indicates the need for more frictional control in models that attempt a simulation of the equatorial currents.)

Energy spectra do not differ much between the two subtropical bands (Fig. 14b,c). In contrast to the more wavelike equatorial regime, effects of higher resolution are not confined to the excitation scale of the eddies but distributed over all wavenumbers. Particularly in the fine-grid case, three wavenumber regimes may be distinguished: an energy-containing band with a very flat spectrum at lower wavenumbers, an inertial range with a power-law dependency close to -3, and a dissipation range at higher wavenumbers where spectral density becomes a more rapidly decreasing function of wavenumber. The latter transition is rather gradual, but frictional control seems to become dominant for wavelengths shorter than about 80–100 km in the fine-grid case, and twice that value in the coarse-grid case. The different resolution seems to have little influence on the cutoff wavenumber, indicating that the energetic fluctuations of 450–500-km wavelength are rather well resolved even by the coarser 1/3° grid. However, the spectral separation between the energetic eddy scale and the scale where friction becomes important is much narrower with the coarse grid and leads to a less clear development of an inertial subrange. This is even more obvious in the subpolar area (Fig. 14a) where the energetic scale is about 170 km, that is, already strongly influenced by the model friction in the coarse-grid case. A tendency toward a k^{-3} subrange begins to show up with the opening of the spectral window between the eddy and the frictional scale in the fine-grid solution.

The cutoff wavelength (λ_c) of 450–500 km in the subtropics is slightly less than twice the wavelength ($2\pi R_1$) of the first-mode Rossby radius (R_1), being 40–50 km in the subtropical model gyre (see Cox 1987); the latitudinal decrease of λ_c corresponds to the decrease of R_1. The spectral characteristics of the model appear analogous to the properties of the Kraichnan (1967) and Batchelor (1969) analyses of two-dimensional turbulent decay, and Charney's (1971) generalized theory of geostrophic turbulence. The model

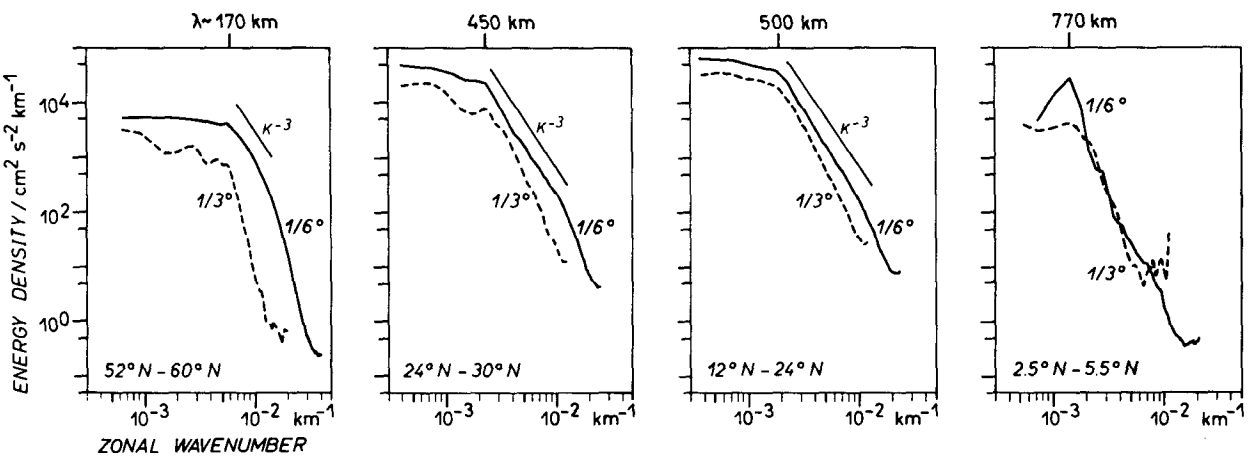

FIG. 14. Energy density of instantaneous velocity as function of zonal wavenumber, derived along zonal sections and averaged in time, for the fine-grid case (solid lines) and the coarse-grid case (dashed lines).

spectra are consistent with the assumption of an eddy generation by baroclinic instability near the principal energy-containing scale, and a kinetic energy spectrum proportional to the -3 power due to an enstrophy cascade to smaller scales. There is abundant evidence for the existence of a spectral dependence close to k^{-3} for atmospheric motions at synoptic-scale wavelengths (e.g., Boer and Shepherd 1983). Evidence for the ocean is rather sparse, but surface height spectra consistent with the predictions of geostrophic turbulence were indicated by the satellite altimeter analysis of Fu (1983) and Fu and Zlotnicki (1989), for the more energetic areas of the World Ocean. These studies and a similar analysis for the North Atlantic by LeTraon et al. (1990) indicate smaller spectral slopes in less energetic areas. However, a recent evaluation of Geosat data for the Atlantic Ocean by Stammer and Böning (1992) suggests that deviations from K^{-3} spectral shapes are confined to those regions where the oceanic signal is not significantly larger than the measurement noise.

A quantitative measure of the dominant eddy scales in the model basins may be obtained from the velocity autocorrelation functions, which were calculated along the same zonal sections as the spectra. (Very similar values are obtained when basing the analysis on the lag of the first zero crossing of the transverse velocity correlations.) Figures 15a and 15b show the integral scales of the longitudinal velocity correlation for two regions as function of depth: the subtropical latitude band between 24° and 30°N, and the subpolar band between 52° and 60°N. In the subtropical gyre there is a sharp decrease of the eddy scales below the main thermocline, probably an effect of the rough-bottom topography that leads to a decoupling of the thermocline and deeper flow field (B89); vertical coherence is larger in the weakly stratified subpolar area. Figure 15c shows the average length scale of the upper 500-m depth, from all four regions, as a function of latitude. The general feature is that the discrepancy between the model cases is growing with latitude. The coarse-grid model reproduces the energetic scale of the fine-grid solution in the subtropics, but clearly fails to simulate the smaller scales at higher latitudes. This appears consistent with the behavior of the 1/3° North Atlantic model. Figure 15d reproduces the latitudinal dependence of the CME model scales in comparison to the numbers derived from the Geosat altimeter data by Stammer and Böning (1992). There is a close model–data correspondence in the subtropics, but a growing discrepancy poleward of about 35° latitude.

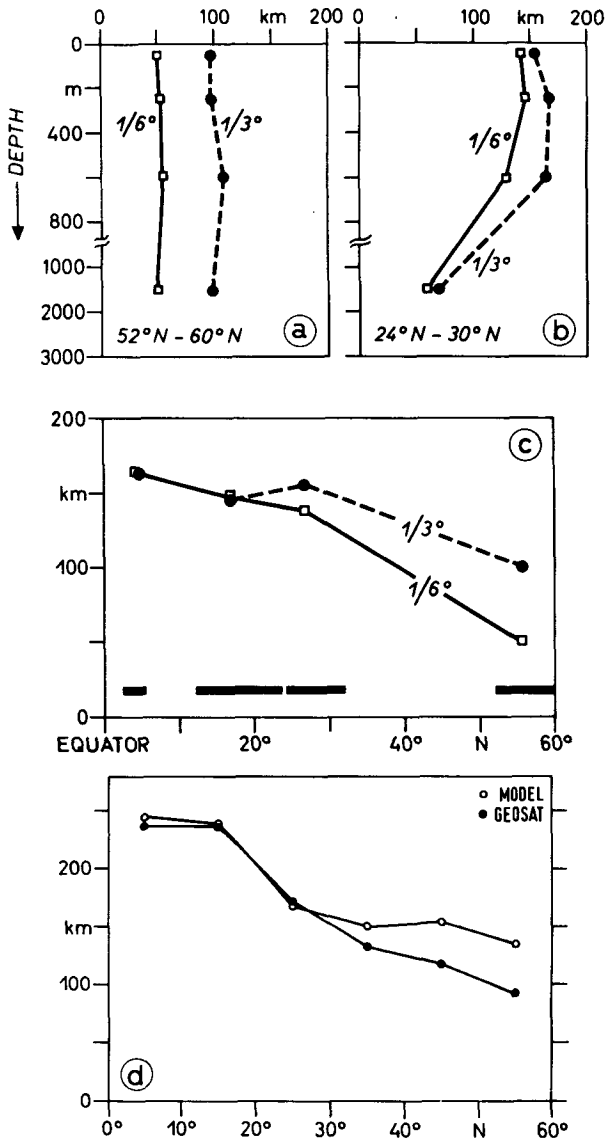

FIG. 15. Characteristic eddy length scales for the coarse- and fine-grid case, calculated from autocorrelation functions of instantaneous velocity along the same zonal sections as in Fig. 14. Shown is (a) the depth dependence in the subtropical gyre, (b) in the subpolar gyre, and (c) the latitudinal dependence of the length scale, vertically averaged over the upper 500 m. The eddy scales are defined here as integral length scales of the longitudinal (zonal) velocity component; results are very similar for the lag of the first zero crossing of the transverse (meridional) velocity component. In (d) the scales of the surface height anomalies found in the 1/3° × 0.4° CME model are compared with scales derived from the Geosat altimeter data for the North Atlantic (adapted from Stammer and Böning 1992). The length scale shown represents the lag of the first zero crossing of alongtrack (Geosat) and meridional (model) autocorrelation over 10° × 10° areas, zonally averaged across the width of the basin.

6. Poleward heat transport

Since the effect of salinity on density is ignored in the box models, the transport of heat is equivalent to the transport of buoyancy. Both terms will be used synonymously here. Mesoscale eddies can contribute to the mean northward transport of heat, $\overline{vT}$, in two ways: by mean eddy fluxes, $\overline{v'T'}$; and by mean momentum fluxes, which may affect the mean velocity field $\bar{v}$ and, thereby, lead to alterations of the heat

transport by the mean flow, $\bar{v}\bar{T}$. In C85, notable contributions of the eddy fluxes were confined to the subtropical gyre region between 10° and 30°N. A remarkable feature of Cox's model solution was that the total heat transport, $\overline{vT}$, remained nearly the same as in a reference solution of lower resolution (1° × 1.2°) without eddies: The eddy transports $\overline{v'T'}$ in the 1/3° model were nearly exactly compensated by an additional transport due to the mean flow, $\bar{v}\bar{T}$. In an analysis of that model, Bryan (1986) noted similarities of the nonbuoyancy transport behavior of the model eddies with the dynamics of transient disturbances in the lower stratosphere. In both cases (and in contrast to tropospheric conditions), nonadiabatic processes can generally be considered as weak, that is, having much longer time scales than the transients. Under adiabatic conditions the nonacceleration theorem applies, and there is no net effect of transients on the mean flow (Andrews and McIntyre 1976).

Figure 16 gives a comparison between the coarse- and fine-grid solutions with respect to the meridional eddy flux of heat. Figures 16a,b show the meridional distribution of $\overline{v'T'}$ in the eastern portion of the basin, zonally averaged between 40° and 50°E. Heat flux by the eddies is generally weak except for the areas of enhanced eddy activity between 10° and 30°N, and near 50°N. In both areas the eddy fluxes are mainly downgradient across the sloping isotherms (see Fig. 3), corresponding to the release of mean potential energy by baroclinic energy transfers in these regions. Eddy fluxes in the southern part of the subtropical thermocline are equatorward, except for the shallowest levels (<100 m depth). Both depth ranges show an only moderate increase of eddy fluxes in the fine-grid case. Differences between the model cases are more pronounced in the subpolar region. Here the eddy fluxes are generally northward and are only weakly depth dependent in the upper 300 or 400 m. Averaged over the area 45°–55°N, 40°–50°E, the eddy flux of 0.17°C cm s^{-1} in the coarse-grid case increases to 0.26°C cm s^{-1} in the fine-grid case, that is, by about 50%.

Much higher eddy heat fluxes are associated with the central jet regime. The meridional pattern of $\overline{v'T'}$, zonally averaged between 10° and 20°E, is illustrated in Fig. 16c,d for the coarse- and fine-grid case, along with an indication of the position of the mean jet axis. In both solutions, eddy fluxes are generally equatorward in the thermocline south of the jet; the southward flux in the fine-grid case (−6°C cm s^{-1}) is about twice the flux found in the coarse-grid model. However, largest differences occur near the jet axis where the very weak values of the coarse-grid solution are replaced by intense northward fluxes, up to 8°C cm s^{-1}.

The contribution of eddy fluxes to the net northward transport of heat, integrated zonally and vertically over the basin, is shown in Fig. 17a for both model cases. The transports in the coarse-grid solution of B89 are

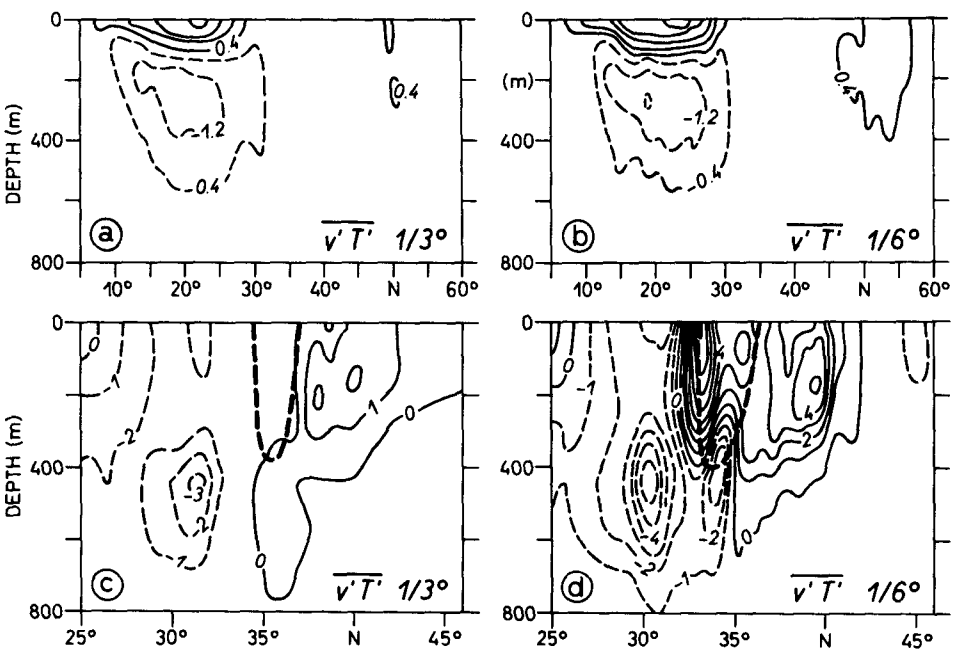

FIG. 16. Eddy flux of heat, $\overline{v'T'}$, (in units of °C cm s^{-1}), for a meridional section in the eastern part of the basin, averaged between 40° and 50°E, for (a) the coarse- and (b) the fine-grid case; and for a section across the central jet, averaged between 10° and 20°E, for (c) the coarse- and (d) the fine-grid case. The heavy dashed line represents the $\bar{u}$ = 20 cm s^{-1} contour.

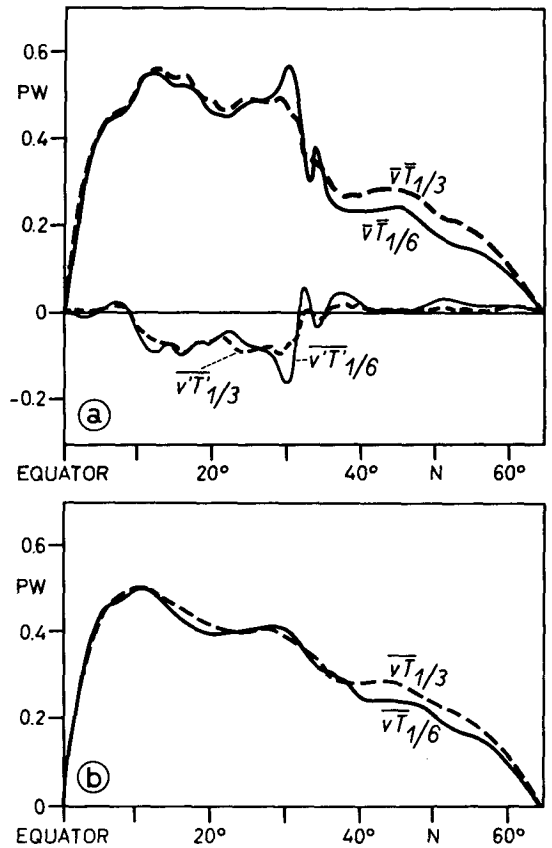

FIG. 17. Northward heat transport in the basin: (a) the contribution of mean flow, $\bar{v}$, $\bar{T}$, and eddies, $\overline{v'T'}$, and (b) the total heat transport, $\overline{vT}$, for the coarse- and fine-grid solution.

The transports in the coarse-grid solution of B89 are very similar to the flat-bottom model of C85. With the finer grid, the eddy transports $\overline{v'T'}$ over the subtropical gyre become not very different, indicating some cancellation between the larger southward transports in the main thermocline and the larger northward transports in the surface layer. The stronger fluxes in the jet area do have an influence on the net eddy transports in the basin. However, the meridional pattern of $\overline{v'T'}$, a negative bump at 30°–31°N and a positive bump at 33°–34°N, has a mirror image in the pattern of the heat transport by the mean flow, $\bar{v}\bar{T}$. Figure 17b indicates an almost perfect compensation between the changes of $\overline{v'T'}$ and $\bar{v}\bar{T}$, leading to a nearly identical heat transport pattern of both model cases south of about 35°N.

The differences in the mean flow leading to the $\bar{v}\bar{T}$ patterns of Fig. 17a are examined in Fig. 18, which shows the zonally integrated, mean meridional transport in the model basin. Figure 18a reveals two basic patterns of overturning motion in the meridional–vertical plane: a signature of the "thermohaline" circulation with deep sinking at the northern wall and maximum strength of 12 Sv (1 Sv $\equiv 10^6$ m^3 s^{-1}); and two counterrotating shallow cells, associated with the wind-driven Ekman transport. The meridional heat transport

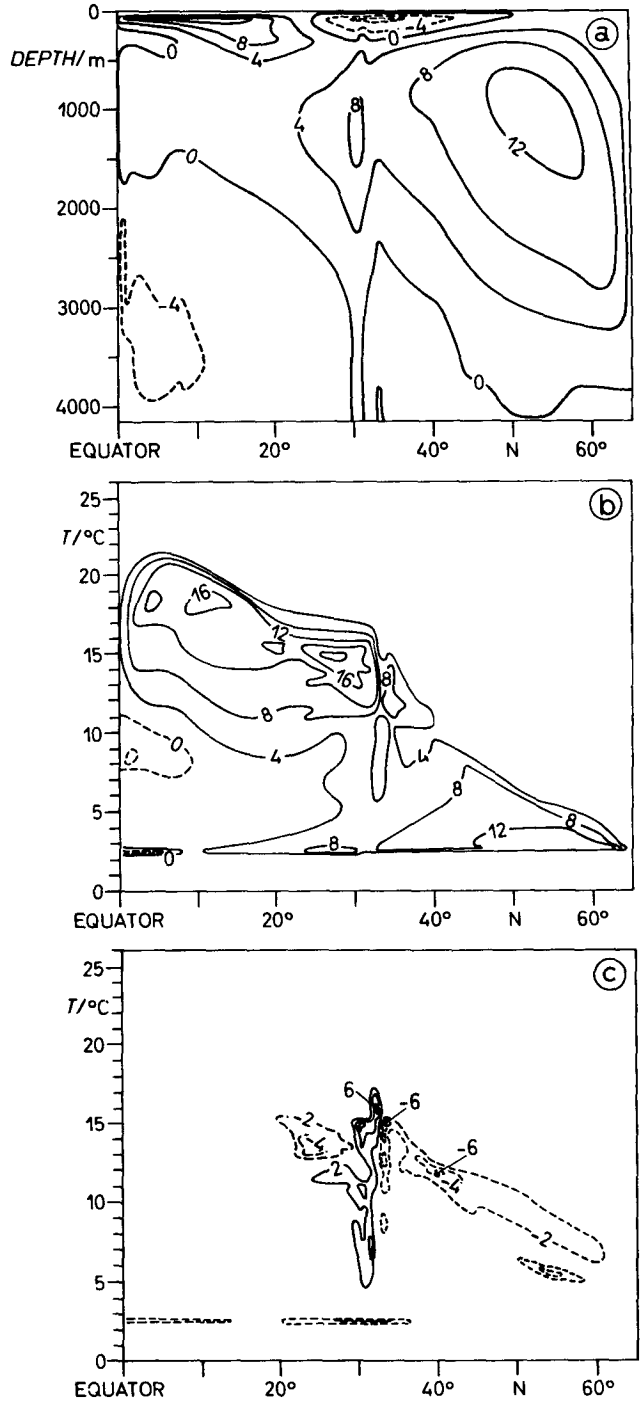

FIG. 18. Mean meridional volume transport for the fine-grid case (a) as function of latitude and depth, (b) as function of latitude and temperature, and (c) its deviation from the coarse-grid solution. Units are 10^6 m^3 s^{-1}.

of these closed cells is proportional to the temperature difference between the upper and lower branches. As shown by Bryan and Sarmiento (1985), this may be illustrated by plotting the meridional circulation using temperature instead of depth as the ordinate. Figure 18b demonstrates that the northward heat transport in the subtropics is mainly due to the shallow wind-driven cell, with maximum strength of 16 Sv, and a relatively large temperature difference between the northward-flowing water and the southward return flow. The region between 30° and 35°N is characterized by strong transports across isotherms reflecting intense convection near the northern boundary of the subtropical gyre. The difference between the fine- and coarse-grid patterns, shown in Fig. 18c, is strongest in this region. The positive transport anomaly south of the jet axis and the negative anomaly north of the jet region lead to the changes of heat transport $\bar{v}\bar{T}$, which compensate the stronger eddy heat fluxes in the fine-grid case. Another difference between the overturning patterns extends along the surface of the subpolar gyre. The decrease of heat transport by the mean flow, $\bar{v}\bar{T}$, is not compensated here by the somewhat increasing eddy transports of the fine-grid model.

7. Conclusions

The comparison between the coarse- ($1/3° \times 0.4°$) and fine-grid ($1/6° \times 0.2°$) solutions of the primitive equation model reveals a strong increase of the eddy activity, particularly in the central jet regime and over parts of the subpolar gyre. In all extratropical model regions, including the central jet, release of mean available potential energy by baroclinic instability is the dominant mechanism for eddy generation. The work of horizontal Reynolds stresses is significant only near the midlatitude jet and indicates, in the fine-grid case, a tendency for energy transfers preferentially from the eddies to the mean flow.

In general, the sensitivity to grid resolution is higher for the kinetic energy of the fluctuations than for their available potential energy. Whereas in the coarse-grid case the ratio $(\mathrm{EPE}/\mathrm{EKE})^{1/2}$ varies between 2 (in the subtropical gyre) and 4 (in the subpolar gyre), there is a striking tendency toward a constant ratio of about 2 in all regions of the fine-grid model, suggesting a fixed relation between the dominant eddy scale and the deformation radius. This behavior corresponds to changes of the eddy length scale as estimated from zonal autocorrelation functions. The coarse-grid model does resolve the scale of the energetic eddies in the subtropical gyre, but obviously fails in higher latitudes where the eddy scale of the fine-grid case is smaller by a factor of 2.

Though the basin dimensions of the model are roughly representative of the North Atlantic Ocean, several idealizations, like the simplified basin geometry and forcing functions, lead to severe distortions of the mean flow and eddy pattern and prohibit a quantitative validation of the model results by comparison of these fields with corresponding observations. However, there are some apparently "universal" features of the oceanic mesoscale variability of strong dynamical implication that may be used to differentiate between the solutions and assess the importance of grid resolution:

- Alongtrack wavenumber spectra from altimeter analysis indicate spectral slopes corresponding to the theory of geostrophic turbulence (Charney 1971) as a universal characteristic of mesoscale variability in the Atlantic Ocean; exceptions are found only in regions with small signal to noise ratios and thus may not represent an oceanic signal (Stammer and Böning 1992). Except for the near-equatorial belt, the model generally predicts zonal wavenumber spectra with slopes close to -3 if resolution is high enough to provide a sufficient separation between the energetic scale and the scale where friction becomes important. In the subtropical gyre this is true for both the fine-grid and the coarse-grid case, and in higher latitudes only for the fine-grid case.
- Both in situ data (Nishida and White 1982; Schmitz 1977, Schmitz et al. 1982) and altimeter observations (Tai and White 1990) suggest a general tendency for the off-diagonal component of the Reynolds stress tensor to obtain positive values south and negative values north of open ocean jets like the Kuroshio and Gulf Stream extensions. The present model shows a similar pattern of $\overline{u'v'}$ only in the fine-grid case.

Despite the strong differences in these signatures of eddy dynamics between the model cases, there seems to be no substantial effect of the fluctuations on the mean northward transport of heat. The stronger eddy intensity in the fine-grid case leads to only small changes of the equatorward heat transport in the subtropics. Strongest eddy fluxes occur across the midlatitude jet, but are almost totally compensated by changes in the mean flow, leaving the total heat transport basically unchanged as compared to the noneddy-resolving reference solution of C85. However, results of the present model can be considered only as preliminary in this respect and have to be interpreted with much caution. As noted by Bryan (1986), heat transport in the idealized model is identical with buoyancy transport. Hence, eddy mixing along isopycnals can lead only to transport of heat in the presence of temperature gradients on the isopycnal surface. To which extent the salinity effect on density, especially in higher latitudes, might exert a significant influence on the transport properties of the eddies remains to be examined. As demonstrated by the model experiments presented here, examination of the role of eddies in middle and

higher latitudes requires a model of the thermohaline circulation with a grid size significantly smaller than 1/3°. Moreover, the quantitative differences between the two solutions in the subtropical gyre—where the 1/3° grid does resolve the first mode Rossby radius—suggests that even a 1/6° model—which does so up to about 45°N—might seriously underestimate the energetic eddy field of the North Atlantic Current.

Acknowledgments. The efforts of R. Gerdes and J. Kielmann to optimize the computational efficiency of the model integration at the CRAY XMP of Kiel University are gratefully appreciated. We thank R. Döscher for helping in the model evaluation. The study was supported by Deutsche Forschungsgemeinschaft, SFB 133.

REFERENCES

Andrews, D. G., and M. E. McIntyre, 1976: Planetary waves in horizontal and vertical shear: Generalized Eliassen-Palm relation and the mean zonal acceleration. *J. Atmos. Sci.*, **33**, 2031–2048.

Barnier, B., B. L. Hua, and C. LeProvost, 1991: On the catalytic role of high baroclinic modes in eddy-driven large-scale circulation. *J. Phys. Oceanogr.*, **21**, 976–997.

Batchelor, G. K., 1969: Computation of the energy spectrum in homogeneous two-dimensional turbulence. *Phys. Fluids*, **12** (Supplement II), 233–239.

Boer, G. J., and T. G. Shepherd, 1983: Large-scale, two-dimensional turbulence in the atmosphere. *J. Atmos. Sci.*, **40**, 164–184.

Böning, C. W., 1989: Influences of a rough bottom topography on flow kinematics in an eddy-resolving circulation model. *J. Phys. Oceanogr.*, **19**, 77–97.

——, and M. D. Cox, 1988: Particle dispersion and mixing of conservative properties in an eddy-resolving model. *J. Phys. Oceanogr.*, **18**, 320–338.

——, R. Döscher, and R. G. Budich, 1991: Seasonal transport variation in the western subtropical North Atlantic: Experiments with an eddy-resolving model. *J. Phys. Oceanogr.*, **21**, 1271–1289.

Bryan, F. O., and W. R. Holland, 1989: A high-resolution simulation of the wind- and thermohaline-driven circulation in the North Atlantic Ocean. Parameterization of small-scale processes, Spec. Publ., Inst. of Geophys., University of Hawaii, 99–115.

Bryan, K., 1969: A numerical method for the study of the circulation of the World Ocean. *J. Comput. Phys.*, **4**, 347–376.

——, 1986: Poleward buoyancy transport in the ocean and mesoscale eddies. *J. Phys. Oceanogr.*, **16**, 927–933.

——, 1987: Potential vorticity in models of the ocean circulation. *Quart. J. Roy. Meteor. Soc.*, **113**, 713–734.

——, and J. L. Sarmiento, 1985: Modeling ocean circulation. *Advances in Geophysics*, Vol. **28A**, Academic Press, 433–459.

Charney, J. G., 1971: Geostrophic turbulence. *J. Atmos. Sci.*, **28**, 1087–1095.

——, and M. E. Stern, 1962: On the stability of internal baroclinic jets in a rotating atmosphere. *J. Atmos. Sci.*, **19**, 159–172.

Cox, M. D., 1984: A primitive equation, 3-dimensional model of the ocean. GFDL Ocean Group Tech. Rep. No. 1, GFDL/Princeton University, 143 pp.

——, 1985: An eddy-resolving numerical model of the ventilated thermocline. *J. Phys. Oceanogr.*, **15**, 1312–1324.

——, 1987: An eddy-resolving numerical model of the ventilated thermocline: Time dependence. *J. Phys. Oceanogr.*, **17**, 1312–1314.

Dantzler, H. L., Jr., 1977: Potential energy maxima in the tropical and subtropical North Atlantic. *J. Phys. Oceanogr.*, **7**, 512–519.

Didden, N., and F. Schott, 1992: Seasonal variations in the western tropical Atlantic: Surface circulation from GEOSAT altimetry and WOCE model results. *J. Geophys. Res.* (in press).

Emery, W. J., 1983: On the geographical variability of the upper level mean and eddy fields in the North Atlantic and North Pacific. *J. Phys. Oceanogr.*, **13**, 269–291.

FRAM Group, The, 1991: An eddy-resolving model of the Southern Ocean. *Eos Trans. Amer. Geophys. Union*, **72**, 169–175.

Fu, L.-L., 1983: On the wave number spectrum of oceanic mesoscale variability observed by the SEASAT altimeter. *J. Geophys. Res.*, **88**, 4331–4341.

——, and V. Zlotnicki, 1989: Observing ocean mesoscale eddies from GEOSAT altimetry: Preliminary results. *Geophys. Res. Lett.*, **16**, 457–460.

——, T. Keffer, P. P. Niiler, and C. Wunsch, 1982: Observations of mesoscale variability in the western North Atlantic: A comparative study. *J. Mar. Res.*, **40**, 809–848.

Gill, A. E., J. S. A. Green, and A. J. Simmons, 1974: Energy partition in the large-scale ocean circulation and the production of mid-ocean eddies. *Deep-Sea Res.*, **21**, 499–528.

Green, J. S. A., 1960: A problem in baroclinic stability. *Quart. J. Roy. Meteor. Soc.*, **86**, 237–251.

Hall, M. M., 1986: A diagnostic investigation of kinetic energy budgets in a numerical model. *J. Geophys. Res.*, **91**, 2555–2568.

Harrison, D. E., and A. R. Robinson, 1978: Energy analysis of open regions of turbulent flows—mean eddy energetics of a numerical ocean circulation experiment. *Dyn. Atmos. Oceans*, **2**, 185–211.

Held, I. M., and D. G. Andrews, 1983: On the direction of the eddy momentum flux in baroclinic instability. *J. Atmos. Sci.*, **40**, 2220–2231.

Holland, W. R., 1985: Simulation of mesoscale ocean variability in mid-latitude gyres. *Advances in Geophysics*, Vol. 28A, Pergamon 479–523.

——, and W. J. Schmitz, Jr., 1985: On the zonal penetration scale of model mid-latitude jets. *J. Phys. Oceanogr.*, **15**, 1859–1875.

——, D. E. Harrison, and A. J. Semtner, Jr., 1983: Eddy-resolving numerical models of large-scale ocean circulation. *Eddies in Marine Sciences*, A. R. Robinson, Ed., Springer-Verlag, 379–403.

Keffer, T., 1983: The baroclinic stability of the Atlantic North Equatorial Current. *J. Phys. Oceanogr.*, **13**, 624–631.

Kraichnan, R. H., 1967: Inertial subranges in two-dimensional turbulence. *Phys. Fluids*, **10**, 1417–1423.

Krauss, W., and R. H. Käse, 1984: Mean circulation and eddy kinetic energy in the eastern North Atlantic. *J. Geophys. Res.*, **89**(C3), 3407–3415.

LeTraon, P. Y., M. C. Rouquet, and C. Boissier, 1990: Spatial scales of mesoscale variability in the North Atlantic as deduced from GEOSAT data. *J. Geophys. Res.*, **95**(C11), 20 267–20 286.

Lorenz, E. N., 1955: Available potential energy and the maintenance of the general circulation. *Tellus*, **2**, 157–167.

McDowell, S. E., P. Rhines, and T. Keffer, 1982: North Atlantic potential vorticity and its relation to the general circulation. *J. Phys. Oceanogr.*, **12**, 1417–1436.

Nishida, H., and W. B. White, 1982: Horizontal eddy fluxes of momentum and kinetic energy in the near-surface of the Kuroshio Extension. *J. Phys. Oceanogr.*, **12**, 160–170.

Oort, A. H., S. C. Ascher, S. Levitus, and J. P. Peixóto, 1989: New estimates of the available potential energy in the World Ocean. *J. Geophys. Res.*, **94**, 3187–3200.

Pedlosky, J., 1979: *Geophysical Fluid Dynamics.* Springer-Verlag, 624 pp.

Reid, R. O., B. A. Elliot, and D. B. Olson, 1981: Available potential energy: A clarification. *J. Phys. Oceanogr.*, **11**, 15–29.

Schmitz, W. J., Jr., 1977: On the deep general circulation in the western North Atlantic. *J. Geophys. Res.*, **81**, 4981–4982.

——, P. P. Niiler, R. L. Bernstein, and W. R. Holland, 1982: Recent long-term moored instrument observations in the western North Pacific. *J. Geophys. Res.*, **87**, 9425–9440.

Schott, F. A., and C. W. Böning, 1991: The WOCE model in the western equatorial Atlantic: Upper layer circulation. *J. Geophys. Res.*, **96,** 6993–7004.

Semtner, A. J., and R. M. Chervin, 1988: A simulation of the global ocean circulation with resolved eddies. *J. Geophys. Res.*, **93,** No. C12, 15 502–15 522.

Spall, M. A., 1990: Circulation in the Canary Basin: A model/data analysis. *J. Geophys. Res.*, **95,** 9611–9628.

Stammer, D., and C. W. Böning, 1992: Mesoscale variability in the Atlantic Ocean from GEOSAT altimetry and WOCE high resolution numerical modelling effort. *J. Phys. Oceanogr.*, **22,** in press.

Tai, C.-K., and W. B. White, 1990: Eddy variability in the Kuroshio Extension as revealed by Geosat altimetry: Energy propagation away from the jet, Reynolds stress, and seasonal cycle. *J. Phys. Oceanogr.*, **20,** 1761–1777.

Treguier, A. M., 1991: Kinetic energy analysis of an eddy-resolving, primitive equation North Atlantic model. (Submitted for publication).

Wood, R. A., 1988: Unstable waves on oceanic fronts: Large-amplitude behavior and mean flow generation. *J. Phys. Oceanogr.*, **18,** 775–787.